Acta Materialia 308 (2026) 121977

Contents lists available at ScienceDirect

Acta Materialia

journal homepage: www.elsevier.com/locate/actamat

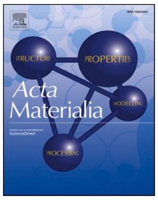

Thermal stability and ion irradiation response of refined grained V – 4Cr – 4Ti

Skye Supakul [a,*], Eda Aydogan [a], Mert Efe [a], Matthew Vigil [b], Bochuan Sun [c], Ishtiaque Robin [a], Kayla Yano [a], Wei-Ying Chen [d], Damian Sobieraj [e], Jan S. Wróbel [e], Duc Nguyen-Manh [f,g], Enrique Martinez [c,h], Dan Thoma [b], Stuart Maloy [a], Osman El-Atwani [a,*]

[a] *Pacific Northwest National Laboratory, Richland, WA, USA*
[b] *University of Wisconsin-Madison, Department of Materials Science and Engineering, Madison, WI, USA*
[c] *Department of Materials Science and Engineering, Clemson University, Clemson, SC, USA*
[d] *Argonne National Laboratory, Lemont, IL, USA*
[e] *Faculty of Materials Science and Engineering, Warsaw University of Technology, Poland*
[f] *Materials Division, United Kingdom Atomic Energy Authority, Culham Campus, Abingdon, United Kingdom*
[g] *Department of Materials, University of Oxford, Parks Road, United Kingdom*
[h] *School of Mechanical and Automotive Engineering, Clemson University, Clemson, SC, USA*

ARTICLE INFO

Keywords:
Ion irradiation
TEM
Thermal stability
Nanoindentation

ABSTRACT

Vanadium-based alloys such as V-4Cr-4Ti are of interest as candidates for low activation structural materials for advanced nuclear reactors. One of the major challenges of vanadium-based alloys is their thermal stability and improving their mechanical properties at higher temperature ranges (> 600°C). This work explores refining the grain microstructure of V-4Cr-4Ti by arc melting and subsequently large strain extrusion machining specimens to produce a multimodal microstructure largely composed of nanocrystalline and ultrafine grain sizes. *In-situ* thermal stability of the multimodal V-4Cr-4Ti to 800°C shows the formation of vanadium carbides with negligible grain growth. *In-situ* dual-beam 16 KeV He^{+} and 1 MeV Kr^{2+} ion irradiation performed at 700°C to a final dose of ~5 displacements per atom show the formation of small cavities well distributed throughout the system, with preferential clustering at grain boundaries. This work provides insight into how the increased fraction of grain boundaries affect the simultaneous dual beam ion irradiation response of multimodal V – 4 wt.% Cr – 4 wt.% Ti at elevated temperatures. Analysis of the cavities reveal an areal density of 0.024 ± 0.007 cavities/nm^2 and swelling of 0.236% after the dual-beam ion irradiation. Nanoindentation shows a ~50% increase in hardening after the ion irradiation at 700°C.

1. Introduction

Since the 1960s, there has been significant interest in vanadium-based alloys as low-activation materials for nuclear reactor operations. Initially considered as candidates for liquid metal-cooled fast reactors, vanadium-based alloys have recently gained renewed attention as alternatives to reduced activation ferritic/martensitic (RAFM) steels for first wall and blanket materials in fusion energy systems due to their limited operating regimes [1–6]. Vanadium-based alloys, such as V-4Cr-4Ti (V44), exhibit desirable thermo-mechanical properties, including a higher melting temperature and promising thermal conductivity compared to other candidate materials like 316 stainless steel (SS) and HT-9 [7]. With the low neutron absorption cross-section of V44, it has also been proposed in self-cooled vanadium (V)/lithium (Li) blanket design concepts, which can achieve the necessary tritium breeding ratio required for sustained reactor operation without requiring the addition of beryllium (Be) [6]. In terms of radioactivity and afterheat decay, high-purity V44 is generally categorized as Class A waste, decaying to acceptable levels during site occupancy. In contrast, V44 of commercial quality or lower purity could be classified as Class B or Class C nuclear waste, which stabilizes and decays to safe levels within 100 years or 500 years, respectively.

---

* Corresponding authors.
E-mail addresses: skye.supakul@pnnl.gov (S. Supakul), osman.elatwani@pnnl.gov (O. El-Atwani).

https://doi.org/10.1016/j.actamat.2026.121977
Received 26 November 2025; Received in revised form 21 January 2026; Accepted 29 January 2026
Available online 31 January 2026

In addition to promising neutronic properties, V44 also possesses a low thermal expansion coefficient across various temperatures. However, V44 alloys have exhibited susceptibility to embrittlement with high levels of hydrogen and oxygen, as well as a reduction in elongation and irradiation work hardening which have largely been attributed to the formation of high densities of irradiation defects and precipitates [8, 9]. Also, the mechanical properties of vanadium-based alloys can vary significantly due to the presence of impurities such as carbon (C), oxygen (O), and nitrogen (N) [10]. Fine precipitates of vanadium carbide [11] and Ti (C, O, N) [9,12,13] have been reported in the literature, forming after heat treatment and irradiation at elevated temperatures. Consequently, extensive research has focused on investigating the effects of impurities and controlling their levels [9,14–16]. Furthermore, studies have explored the influence of various elements and particles, such as Fe, Si, ZrC, TiC, Ti_3SiC_2, and Y-based oxides, on strength, ductility, and creep resistance [15,17,18]. Others have also investigated the thermo-mechanical processing of V44 through aging, deformation, and annealing [9,11,12,19], observing banded microstructures with fine grains, alongside the formation of precipitates as a result of aging. The formation of these bands leads to inhomogeneities in the mechanical performance of the system. When subjected to ion irradiation at elevated temperatures, the microstructure can become unstable due to the breakdown of Ti (C, O, N) and the formation of V (C, O, N), attributed to the redistribution of carbon throughout the system.

To implement vanadium-based alloys as structural materials, further work is required to modify the microstructure and control the impurity content in the system. In addition, there is significant interest in the community to improve the operating temperature window of vanadium alloys, aiming to improve their high temperature strength and creep properties [6]. Apart from different alloying additions and oxide or precipitate strengthening, microstructural modifications serve as another technique to improve the performance of a material. Various groups have employed a series of multi-step thermomechanical treatments (TMT) to modify V44 [11,20–22]. Moreover, there has been only a limited number of studies discussing the ion irradiation behavior of ultrafine-grained or nanocrystalline V44 [11]. Work on modifying tungsten to produce nanocrystalline grains using large strain extrusion machining (LSEM) has demonstrated reductions in the areal density of cavities, defect clusters, and dislocations, as compared to ultrafine-grained tungsten [23,24]. Additionally, increased strength, while retaining much of the ductility, has been observed with grain and precipitate refinement in TMT modified V44 [21]. Thus, the present study utilized LSEM to refine the grain microstructure of V44, producing LSEM V44 with a multimodal grain size distribution, ranging from nanocrystalline to coarse grain sizes. *In-situ* high-temperature transmission electron microscopy (TEM) investigations were performed to gain insight into the thermal stability of nanocrystalline V44 at temperatures up to 800°C. Furthermore, simultaneous dual-beam ion irradiation using 16 keV He^+ and 1 MeV Kr^{2+} at an elevated temperature of 700°C was conducted to evaluate the irradiation tolerance of multimodal grain-sized V44. Nanoindentation was performed before and after irradiation to investigate the ion irradiation hardening behavior, revealing a ~50 % increase in hardening after ion irradiation.

2. Materials and methods

2.1. *Arc meltingand LSEM of V – 4 wt. % Cr– 4 wt. % Ti*

Ingots were prepared by arc-melting using an Arcast Arc 200. Shots of pure elements of V (99.9 %), Ti (99.9 %), and Cr (99.95 %) were melted together on a water-cooled copper crucible in an ultra-high purity Ar (99.999 %) environment. The chamber was evacuated to $\sim 2.7 \times 10^{-4}$ kPa and back-filled to ~35 kPa with ultra-high purity Ar three times to minimize O and N contamination. In addition, a Ti getter ingot was melted prior and adjacent to the ingots. This process was repeated at least four times, flipping the ingot each time to ensure complete mixing. The Ti getter and samples were lustrous with no discoloration and minimal mass lost between melts. The final weight of the ~1″ diameter ingot was approximately 40 g. Initial microstructure of the coarse grain (CG) arc melted specimen is shown in Supplemental Fig. S1, with grain sizes of 402±190 μm in terms of equivalent area diameter.

Nanocrystalline V44 alloy chips and semi-continuous strips were produced by the large strain extrusion machining (LSEM) process, which peeled/machined the chips from the as-cast V44 buttons in a lathe. With LSEM, large strains can be imposed in a narrow and confined shear deformation zone between the cutting tools to refine microstructures to the ultrafine and nanocrystalline level. The other thermo-mechanical conditions such as strain rate and temperature can also be modeled and controlled in the deformation zone as accurate as strain. Since machining is a high strain rate process by its nature, adiabatic heating due to the large plastic deformation can cause a local temperature rise in the deformation zone. The temperature rise in the deformation zone was calculated and reported, even though all the machining was done at room temperature without the preheating of the disc [25].

The effective strain $\bar{\varepsilon}$ imposed on the strips can be calculated by Eq. 1 which idealizes the deformation zone as a single shear plane:

$$\bar{\varepsilon} = \frac{\gamma}{\sqrt{3}} \tag{1}$$

where γ is the shear strain. Shear strain is calculated by using Eq. 2 below:

$$\gamma = \frac{\lambda}{\cos\alpha} + \frac{1}{\lambda\cos\alpha} - 2\tan\alpha \tag{2}$$

where α is the tool rake angle and λ is the chip or strip thickness ratio. The strip thickness ratio is t_c/t_0, where t_c and t_0 are the final and the uniformed chip thicknesses respectively. In LSEM, an optional constraining tool can be used to control the final strip thickness. There was no constraining tool used in this study, and the final strip thickness naturally formed as a result of the shear strain imposed on the material and its relative ductility.

Strain rate $\dot{\bar{\varepsilon}}$ is approximated using a deformation zone thickness (Δ) and deformation speed (V) in Eq. 3 below:

$$\dot{\bar{\varepsilon}} \sim \frac{\bar{\varepsilon}V}{\Delta} = \frac{\gamma V}{\sqrt{3}\Delta}. \tag{3}$$

The average deformation zone temperature (T) can be estimated using the shear plane model which converts the cutting energy to the adiabatic deformation heating and calculates the fraction of heat flowing into the work material by considering the work material's heat capacity, thermal conductivity, density, and the shear plane component of the cutting force. The physical properties used to calculate the temperature are based on the reported values for pure vanadium, where heat capacity, $C = 0.49$ J/gK, thermal conductivity, $\kappa = 35$ W/mK, and density, $\rho = 6.11$ g/cm^3. The specific cutting energy (u_s) was assumed to be similar to steels with $u_s = 2.9 \times 10^9$ J/m^3. Table 1 summarizes the process parameters used in this study and the strain, strain rate, and temperature that the strip experienced during the LSEM process.

Impurity analysis of C, O, and N was performed on the as-cast coarse grain V44 and after LSEM processing by Luvak, inc. following ASTM E - 1019–24 (Oxygen & Nitrogen– Inert Gas Fusion and Carbon – Combustion Infrared Detection) standards. For the as-cast CG V44, 0.022 wt.

Table 1
LSEM process parameters used to produce the V44 alloy strips and the strain, strain rate, and temperature in the deformation zone during processing.

t_0 (mm)	t_c (mm)	λ	α	γ	$\bar{\varepsilon}$	Δ (μm)	V (m/s)	$\dot{\bar{\varepsilon}}$ (1/s)	T (K)
0.1	0.33	3.3	0°	3.6	2.1	100	1.6	3.1×10^4	1040

% C, 0.1 wt. % O, and 0.003 wt. % N was identified. After LSEM processing, the V44 possessed 0.017 wt. % C, 0.047 wt. % O, and 0.006 wt. % of N.

2.2. Electron microscopycharacterization

Microstructural characterization was performed using a JEOL JSM-IT800 Schottky Field Emission Scanning Electron Microscope (SEM) equipped with an Oxford Ultim Max 170 mm^2 energy dispersive X-ray spectroscopy (EDS) detector at a working distance of 10 mm and operating voltages ranging from 15 – 20 kV. Electron backscattered diffraction (EBSD) was performed using a step size of 1.07 µm, 40 nm, and 15 nm for the EBSD maps at 300x, 5,000x, and 11,000x, respectively. After LSEM, the V44 was punched out into 3 mm diameter discs that were ground with 1200 and 2400 grit SiC paper to ~120 µm thickness. For SEM characterization, some of the 3 mm discs were polished with 6 and 3 µm diamond paste polishing before being finished with an 4:1 solution of Struers OP-S and hydrogen peroxide. Following polishing, samples were sonicated in ethanol and dried under dry air. For transmission electron microscopy (TEM) characterization, some of the 3 mm discs were electropolished until perforation using a 4:1 solution of methanol and sulfuric acid at -10°C in a Struers Tenupol-5. TEM characterization was performed using the JEOL ARM 200CF AC and JEOL GrandARM 300CF AC-Scanning Transmission Electron Microscope (STEM). Sample thicknesses were taken from thickness maps using energy filtered transmission electron microscopy (EFTEM) utilizing an effective atomic number calculated for each specimen using the log-ratio technique [26].

For the *in-situ* TEM heating experiment, a focused ion beam (FIB) equipped on a FEI Quanta dual-beam SEM/FIB was used to prepare a FIB liftout attached to a molybdenum TEM half grid. The lamella was capped with 3 protective layers: electron deposited Pt, ion deposited carbon, and ion deposited Pt. To finish the FIB lamella, both sides were polished with 5 kV, followed by 2 kV Ga ions for a minimum of 2 min. The *in-situ* TEM heating experiment was performed using a Gatan double tilt heating holder, heating the specimen from room temperature to 800°C with a heating rate of 22 °/min. The vacuum of the TEM chamber was $\sim 7 \times 10^{-6}$ Pa after 1 hour. The temperature was held at 800°C for 30 min before cooling the specimen back to room temperature at the same rate as the heating.

2.3. In-situ dual-beamionirradiation

Samples were subjected to *in-situ* heating simultaneous dual-beam ion irradiation using 16 KeV He$^+$ and 1 MeV Kr^{2+} ions at the Intermediate Voltage Electron Microscopy (IVEM) Facility at Argonne National Laboratory [27]. The sample chamber vacuum was $\sim 7 \times 10^{-8}$ Torr. Specimens were heated to 700°C over ~20 min, after which the temperature was momentarily held constant before starting the dual-beam ion irradiation. Samples were subjected to fluxes of 9.3×10^{12} ions•cm^{-2}s^{-1} and 6.3×10^{11} ions•cm^{-2}s^{-1} for He$^+$ and Kr^{2+} ions, respectively, for 3948 s (65 min and 48 s). This equates to fluences of 3.67×10^{16} ions•cm^{-2} and 2.47×10^{15} ions•cm^{-2} for He$^+$ and Kr^{2+} ions, respectively. In terms of dpa, this is expected to be equivalent to ~5 dpa with a He/dpa ratio of ~1.

Damage calculations were performed using the Stopping Range of Ions in Matter (SRIM) 2013 Pro with the Kinchin-Pease model, and results are shown in Supplemental Fig. S2 for the ternary and quaternary systems. Since all constituents of the alloy systems are transition metals, the value of 40 eV was set as the displacement energy for all the elements as suggested by Stoller *et al.* [28]. The value of 40 eV was used in this work to compare and be consistent with other studies [29].

2.4. Modeling and simulations

Metropolis Monte Carlo simulations with a cluster expansion (CE) Hamiltonian and density functional theory (DFT) on $V_{92}Cr_4Ti_4$ (at. %) were performed to gain a deeper understanding of the equilibrium states at different temperatures. The supercell contains 8192 atoms in the form of 16 × 16 × 16 body-centered cubic (BCC) unit cells. The sample was first heated up to 2000 K and then cooled down to 200 K with a temperature decrement of 200 K. To reach equilibrium, we applied 4000 Monte Carlo steps per atom at each temperature, and after the system reached equilibrium, another 5000 Monte Carlo steps per atom were applied to calculate averages for data analysis.

2.5. Ex-situ nanoindentation

Nanoindentation was performed using a Bruker-Hysitron TI Premier I with a standard low load transducer capable of a max load of ~11 mN. Indents were performed in open-loop displacement-controlled mode to a depth of 200 nm using a diamond Berkovich indenter. Both loading and unloading segments were performed with a strain rate of 0.05 s^{-1}. A 10 s hold segment at the peak displacement was used to accommodate creep. Spacing between indents were 10 µm. Hardness values were calculated using 95 % of the peak load and an Oliver-Pharr fit for the tip area function.

For reporting the nanoindentation hardness of the irradiated electropolished 3 mm disc of LSEM V44 at 700°C, 5 by 10 arrays of indents with 20 µm spacing were performed at an arbitrary distance away from the perforation hole in the center of the disc (see Supplementary Fig. S5A). Reported average values of hardness for the irradiated specimen used values after the 100 µm arbitrary distance away from the perforation hole, which is the point at which the hardness values began to stabilize (Supplementary Fig. S5B).

3. Results

3.1. Microstructure of LSEM V44

The microstructure of the V44 after LSEM is shown in Fig. 1. Overall, the EDS maps (Fig. 1B – D), show that the composition is homogeneously distributed with a composition of 92.3 wt. % V, 3.9 wt. % Ti, and 3.8 wt. % Cr (equivalent to $V_{92.1}Ti_{4.1}Cr_{3.8}$ at. %). Diagonal streak-like regions can be observed in the V (Fig. 1B) and Ti (Fig. 1C) maps, regions with a slight enrichment in Ti (~0.4 at. %) and, consequently, depletion in V (see Fig. 1B – C, 1F, region 1) as well as regions enriched in V (~1.7 at. %) and consequently depleted in Ti and Cr (see Fig. 1B – C, 1F, region 2). A plot (Fig. 1E) of the line scan (indicated by the orange arrow in Fig. 1A – C) shows the compositional variation across the various enriched regions. The morphology of diagonal streak-like regions appears throughout the entire region and is suspected to be a result of the LSEM process.

Fig. 1G shows a band contrast image with the associated EBSD map (Fig. 1H) taken at a low magnification of 300x. The EBSD maps show an anisotropic grain microstructure with bands of elongated grains aligning with the diagonal streak-like regions observed in Fig. 1A – C. Within the bands, the grains are not equiaxed and possess some level of texture. Higher magnification EBSD scans were performed at 5,000x (Fig. 1I) and 11,000x (Fig. 1J), highlighting the significant present of submicron grain sizes present in the sample after LSEM. The kernel average misorientation map (Fig. 1K) shows the presence of geometrically necessary dislocations present near a majority of the grain boundaries. This is to be expected with the as-processed LSEM specimen. Fig. 1L shows the multi-modal grain size distribution of the system based on the area-fraction of grain sizes from Fig. 1H, with 30.7 % of the area pertaining to fine grained or below grain sizes, 49.3 % of the area pertaining to coarse grain sizes (5 µm < d < 100 µm, where *d* is the equivalent area grain diameter), and 19.9 % or the area pertaining to large grains (d > 100 µm). Analysis of Fig. 1J gives some insight into the number fraction of fine-grained and below grain sizes with 11.6 % of grains being categorized as fine grained (500 nm < *d* < 5 µm), 53.5 % categorized as

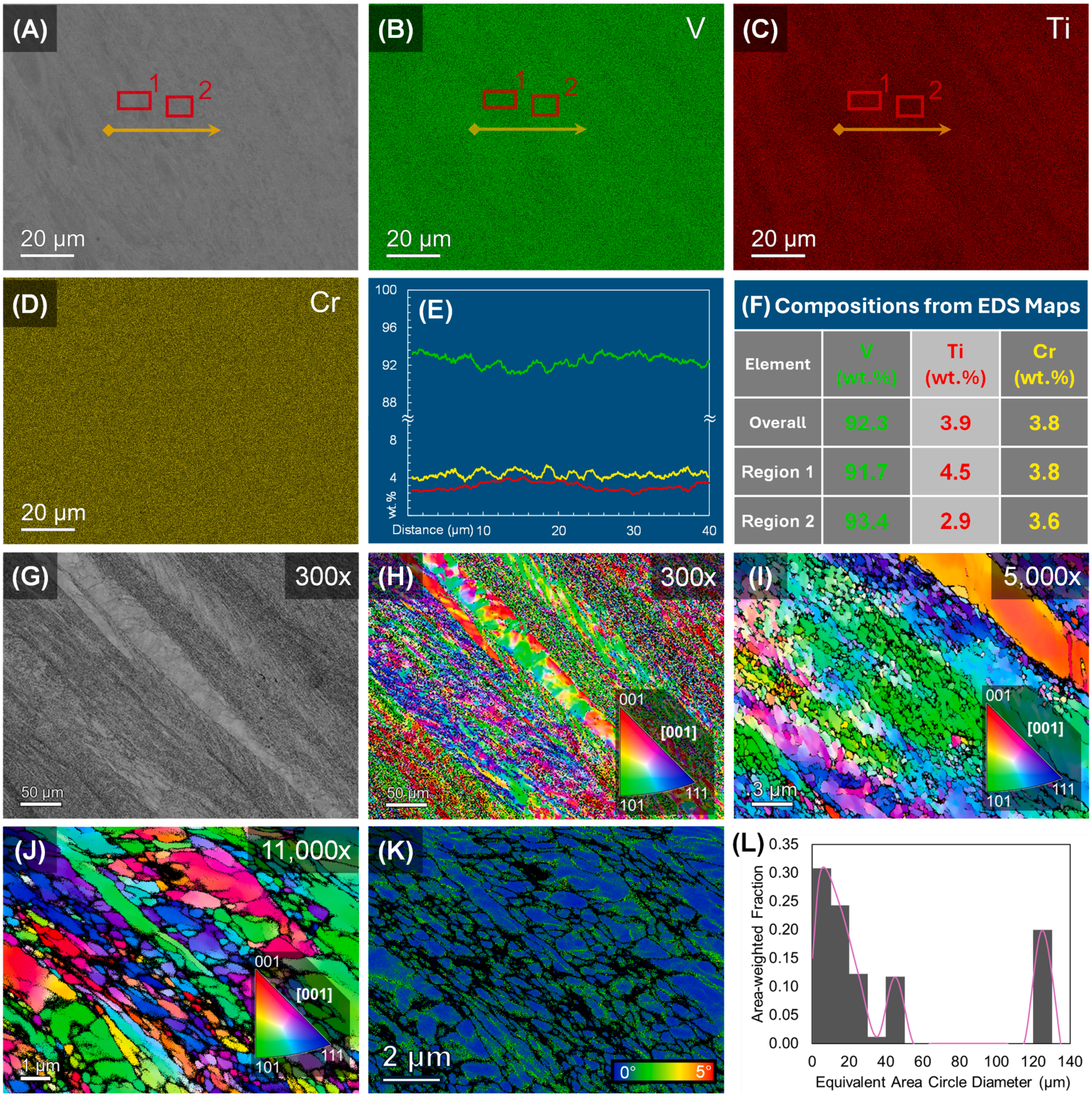

(F) Compositions from EDS Maps

Element	V (wt.%)	Ti (wt.%)	Cr (wt.%)
Overall	92.3	3.9	3.8
Region 1	91.7	4.5	3.8
Region 2	93.4	2.9	3.6

Fig. 1. Backscattered SEM image of the LSEM V44 (A) with associated EDS maps for V (B), Ti (C), and Cr (D). A plot of the line scanned performed over the region indicated by the orange line in (A) is shown in (E). A table of the compositions is shown in (F) from the overall EDS map, as well as region 1 and region 2, as indicated by the red rectangles in (A), showing the variation in composition in and outside of one of the V-rich regions. Band contrast of the nanocrystalline V44 (G) with associated EBSD map (H). Higher magnification EBSD maps are shown, taken at 5,000x (I) and 11,000x (J). The kernel average misorientation map (K) of the region in (J) is shown. (L) shows a plot of the weighted fraction of grains based on the equivalent area circle diameter of the region shown in (H).

ultra-fine grained ($100 < d < 500$ nm), and 34.9 % being categorized as nanocrystalline grains ($d < 100$ nm).

3.2. *Ex-Situ nanoindentation*

Nanoindentation was performed in five different arbitrary regions on the LSEM V44 specimen. Fig. 2A – D show hardness maps of three of the regions, showing a random spread of values. Fig. 2E shows a post nanoindentation EBSD map of the indents indicated in Fig. 2D From the EBSD, some of the indents are expected to have fallen near or on the grain boundaries. Given the large presence of nanocrystalline and ultrafine sized grains, the values shown incorporate these microstructural features. The average hardness across each of the tested regions is shown in Fig. 2F. The hardness value reported represents the hardness at the very center 10 × 10 µm grid cell. Each individual indent is estimated to have a plastic zone radius of ~1150 nm from the center of the grid unit cell. The plastic zone radius could be estimated using equations as described by Woodcock et al. [30], using mechanical properties of V-4Cr-4Ti. The variation of hardness in different regions is attributed to the heterogeneous microstructure with a multimodal grain size distribution. Indents from position 0 and 1 likely landed on coarser grains such as those observed in Fig. 1H For vanadium and many of its alloys, the Zener anisotropy ratio is near 1 [31]. Thus, any texture in the sample is not expected to lead to significant differences in the hardness, indicating the difference in hardness may be attributed to grain size with the presence of grain boundaries, as well as strain hardening from an increased number of dislocations produced by the LSEM process.

From Fig. 2D and E, some correlations could be observed between the hardness value and the microstructure in which the indents landed on. Indents that possessed higher hardness values (such as the top third

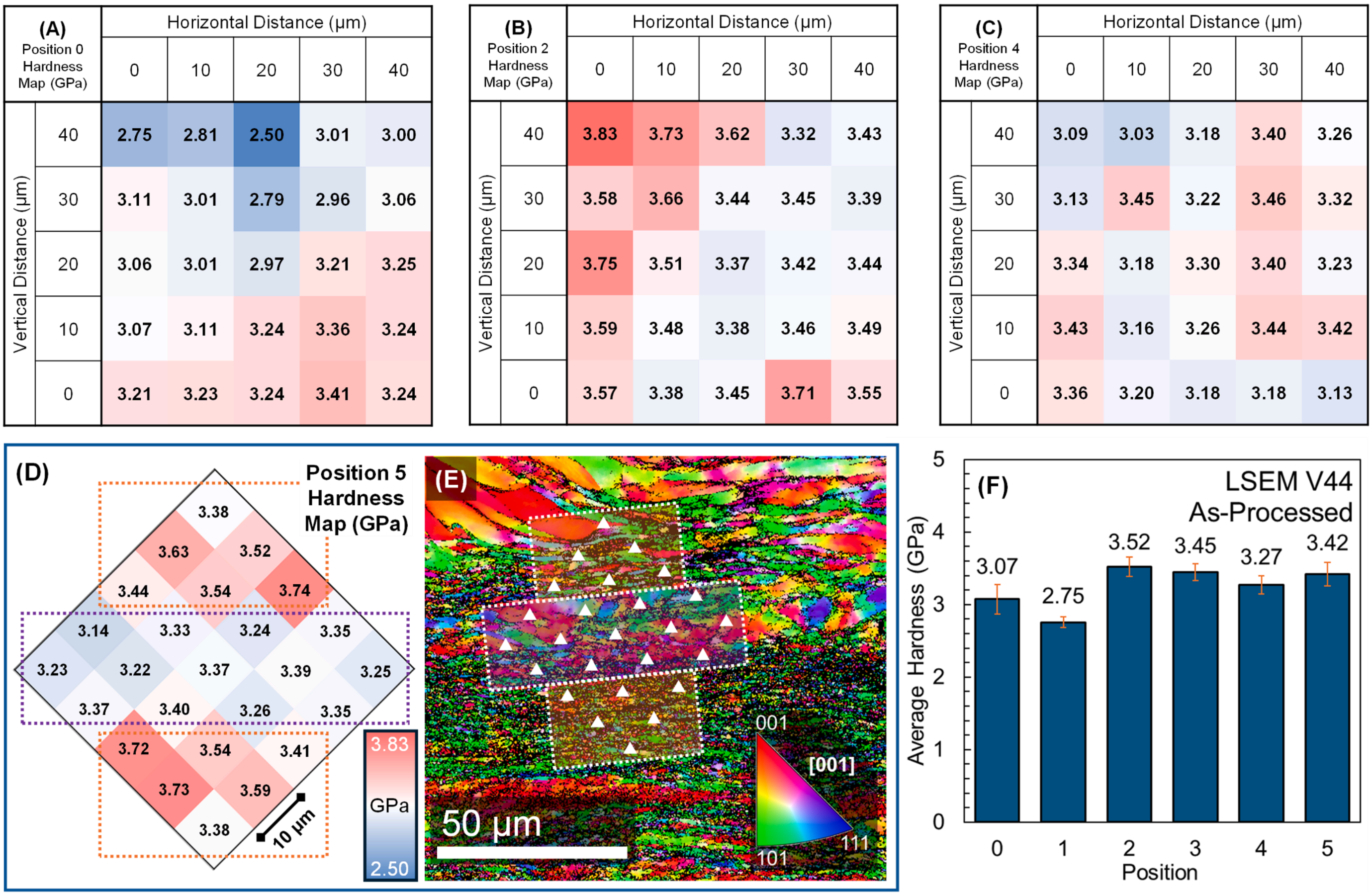

(A) Position 0 Hardness Map (GPa)		Horizontal Distance (µm)				
		0	10	20	30	40
Vertical Distance (µm)	40	2.75	2.81	2.50	3.01	3.00
	30	3.11	3.01	2.79	2.96	3.06
	20	3.06	3.01	2.97	3.21	3.25
	10	3.07	3.11	3.24	3.36	3.24
	0	3.21	3.23	3.24	3.41	3.24

(B) Position 2 Hardness Map (GPa)		Horizontal Distance (µm)				
		0	10	20	30	40
Vertical Distance (µm)	40	3.83	3.73	3.62	3.32	3.43
	30	3.58	3.66	3.44	3.45	3.39
	20	3.75	3.51	3.37	3.42	3.44
	10	3.59	3.48	3.38	3.46	3.49
	0	3.57	3.38	3.45	3.71	3.55

(C) Position 4 Hardness Map (GPa)		Horizontal Distance (µm)				
		0	10	20	30	40
Vertical Distance (µm)	40	3.09	3.03	3.18	3.40	3.26
	30	3.13	3.45	3.22	3.46	3.32
	20	3.34	3.18	3.30	3.40	3.23
	10	3.43	3.16	3.26	3.44	3.42
	0	3.36	3.20	3.18	3.18	3.13

Fig. 2. Nanoindentation maps of three arbitrary regions on the LSEM V44 specimen (A – C). A hardness map (D) associated with the region in the EBSD map (E) is also shown. Inset intensity bar in (D) represents the maximum and minimum values for all the nanoindentation positions, including the maps shown in (A – C). White triangles (not to scale; enlarged for emphasis) indicate the position of the indents in the EBSD map. (F) shows a plot of the average hardness with standard deviation of the different arbitrary positions on the LSEM V44 specimen.

or bottom third of Fig. 2D), appear to have landed in areas with nanocrystalline and ultrafine grains. Meanwhile indents with moderate to low relative hardness values (middle region values of Fig. 2D) landed in regions with relatively coarser grain sizes. This suggests there is a Hall-Petch-like strengthening effect (where hardness increases with decreasing grain size) playing a role in the higher hardness observed in the nanocrystalline and ultrafine grained regions. In addition to the size of the grains, it should be noted that the indentation response in these regions will also be affected the number of grain boundaries present in the region. These will also serve as another strengthening mechanism, where the grain boundaries act as obstacles for dislocation motion as the material plastically deforms under the indent. Due to the highly plastically strained material in the ultrafine and nanocrystalline regions, it is difficult to identify and index all the grains. Further detailed investigations are required to better correlate and understand the relationship between grain size and hardness response.

3.3. In-Situ TEM heating

To gain insight into the thermal stability of this specific grade of V44, in-situ TEM heating was performed on a TEM FIB liftout. Fig. 3A – D shows scanning transmission electron microscope (STEM) bright field (BF) images taken without interrupting the temperature ramp at room temperature, 400°C, 600°C, and 700°C. A red oval marks a feature that was being tracked and evolved during the temperature ramp. From Fig. 3D – F, a larger condenser aperture was used to obtain better contrast in the images. Between 600°C and 700°C, plate-like features began to form (highlighted by the red oval in Fig. 3E). These features remained present at 800°C and stable after 30 min at 800°C. There was no significant change in microstructure of V44 observed during the 30-min hold. A brightfield TEM image (Fig. 3G) was taken at room temperature after the end of the in-situ heating experiment with an associated SAD pattern (Fig. 3H) taken from the region highlighted by the yellow circle in Fig. 3G Elongated, oval precipitates with darker contrasts can be observed throughout the region after the heating experiment. From the SAD pattern, multiple phases and grains can be observed, with multiple diffraction spots being slightly elongated along the diffraction rings. This may indicate two things; first, it suggests the presence of ultrafine and nanocrystalline grains, oxides, and precipitates. Since they are elongated along the diffraction rings, it means that many of the small grains are slightly rotated but still share the same family of planes. This also suggests some texturing with some of the grains observed.

More of the plate-like features can be observed in the annular dark field (ADF) STEM image shown in Fig. 3I. Associated EDS maps (Fig. 3J – M) from the region shows the presence of carbon in these features. A plot (Fig. 3N) of the line scan over the area indicated by the yellow arrow in Fig. 3I suggests that the feature is likely a vanadium carbide. The low value of vanadium measured in the line scan is likely skewed by the presence of carbon being detected throughout the chamber, especially after the in-situ heating in which dust and dirt present on the holder may have been burned off. Vanadium-oxide-rich precipitates can also be observed, separate from the vanadium carbide-rich precipitates. Their presence is further confirmed in the SAD shown in Fig. 3H coming from the region in Fig. 3G as indicated by the dashed yellow circle. Impurities such as carbon, oxygen, and nitrogen have been known to be difficult to

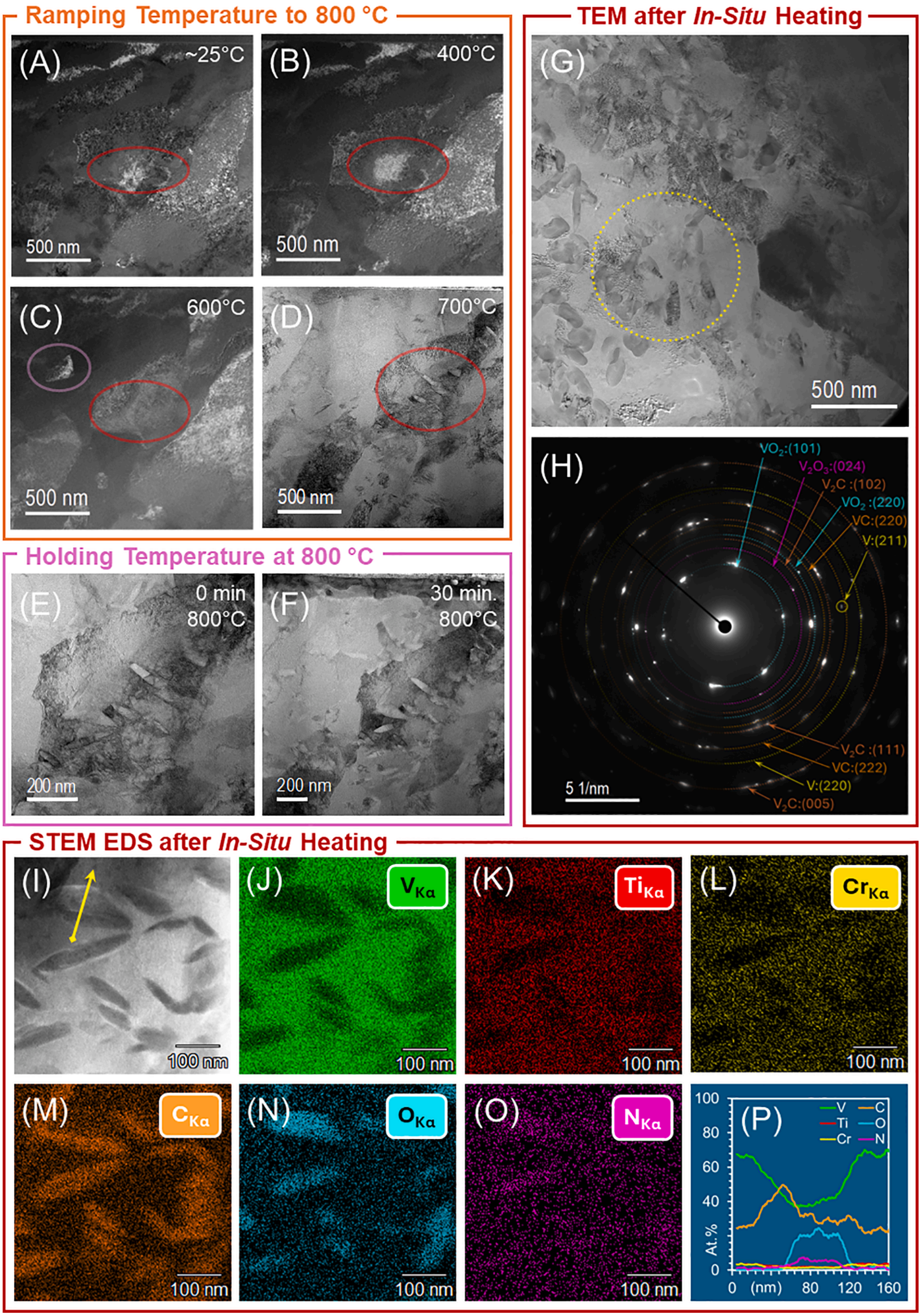

Fig. 3. STEM-BF images of the LSEM V44 taken during the temperature ramp to 800°C at room temperature (a), 400°C (B), 600°C (C), 700°C (D). The red oval highlights a feature evolving with temperature. STEM-BF images were taken at 0 min (E) and 30 min (F) at 800°C. Brightfield TEM image (G) of the LSEM V44 at room temperature after being exposed to 800°C for 30 min with an associated SAD pattern (H) of the region highlighted by the yellow dashed circle in (G). STEM-ADF (annular dark field) images after annealing (I) with associated EDS maps of V (J), Ti (K), Cr (L), C (M), O (N), and N (O). Shown in (P) is a plot of the line scan indicated by the yellow arrow in (I).

eliminate and minimize in the production of V44 alloys [9,10,21], and have been observed to form Ti(C, O, N) and V(C, O, N) at elevated temperatures. From the impurity chemical analysis performed of the LSEM V44 specimen, there is 0.017 wt. % of C, 0.047 wt. % of O, and 0.006 wt. % of N present in the sample. Carbon burned off from the holder or from the protective carbon coating may serve as additional sources of carbon to form carbides during the *in-situ* TEM experiment.

From the in-situ TEM heating experiments, it was determined that this grade of V44 subjected to LSEM forms vanadium carbide after 600°C. Up to 800°C, some indications of recrystallization could be observed, however there was no significant grain coarsening occurring, despite the ultrafine and nanocrystalline grain sizes.

3.4. *Ion irradiation*

Dual beam ion irradiation of 16 KeV He^+ and 1 MeV Kr^{2+} was performed at 700°C, a temperature relevant for advanced nuclear reactor operations, while near the limit for the thermal stability of the multimodal V44. The ion irradiation was recorded and can be observed in Supplemental Video S1. To capture the presence and quantify cavities, underfocused BF-TEM images were taken to produce Fresnel fringe contrast that comes from the phase interference between the material matrix and the cavity interface [32]. Throughout the ion irradiation, there was dynamic formation, migration, and annihilation of defects in the material (see Supplemental Video S1). At 0.5 dpa (Fig. 4A), the presence of small cavities can be observed, with the density of cavities increasing to 5 dpa. At 1 dpa (Fig. 4B), the small cavities can be observed to cluster at grain boundaries (see line of yellow arrows); however, they

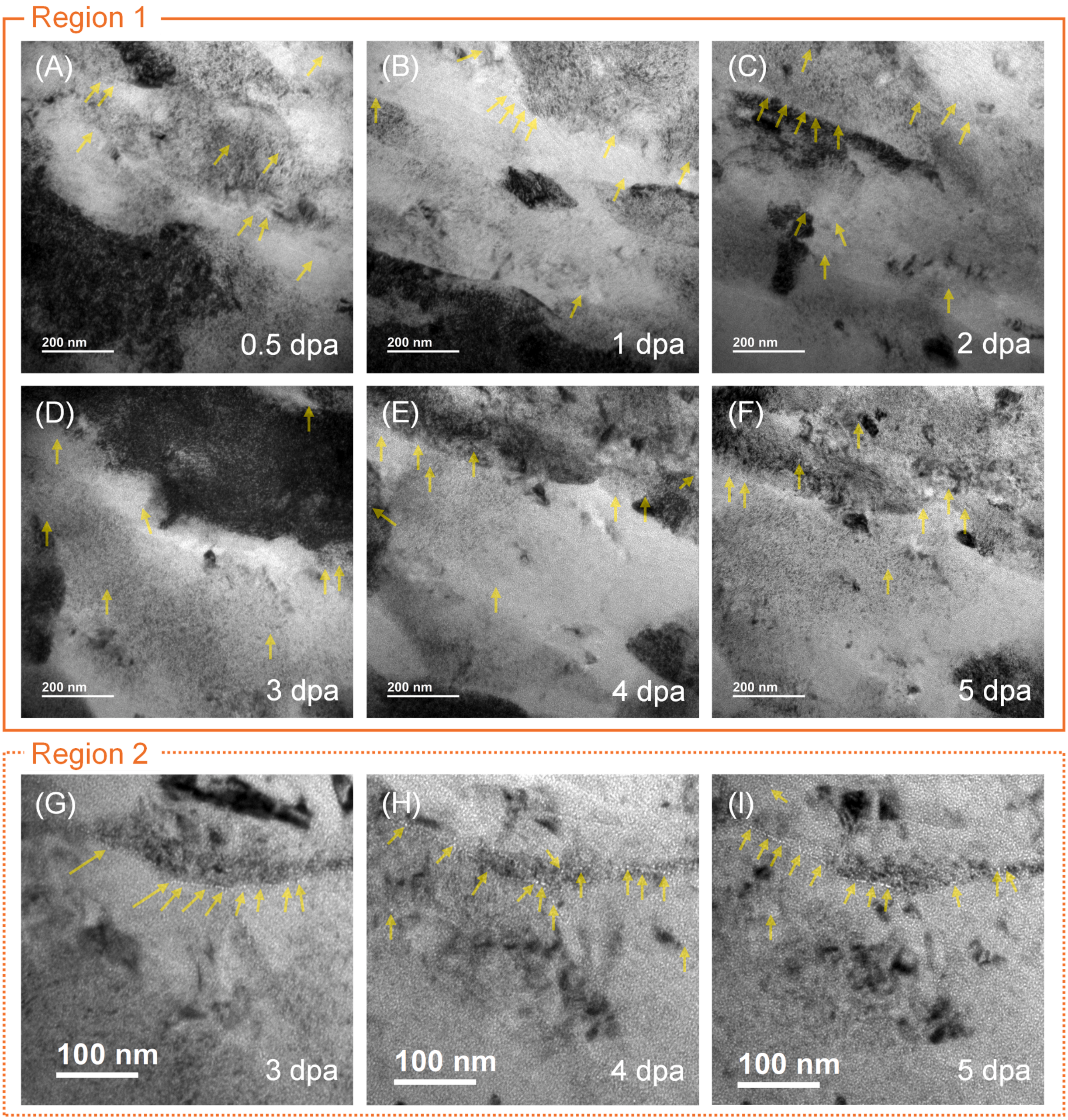

Fig. 4. Underfocused BF-TEM images taken during the in-situ dual-beam ion irradiation 700°C at 0.5 (A), 1 (B), 2 (C), 3 (D), 4 (E), 5 (F) dpa to better visualize the presence of any cavities in the sample. Underfocused BF-TEM images taken at a different region, labeled as region 2, were also taken at 3 (G), 4 (H), and 5 (I) dpa. Distinguishable cavities are noted by the yellow arrows, though the ones highlighted do not represent all the cavities observed in the images.

do not appear to grow significantly in size to 5 dpa (see Fig. 4F, 4I). While there is preferential clustering of cavities at the boundaries, cavities are also seen well distributed throughout the grain matrices. There was no observable dynamic grain growth or recrystallization occurring during the ion irradiation at 700°C.

From the selected area electron diffraction (Fig. 5B) taken from a region in Fig. 5A, most of the diffraction spots correspond well with vanadium, with some spots matching well with vanadium carbide. Orange arrows seen in Fig. 5A point to a handful of identified vanadium carbide precipitates. The presence of multiple vanadium diffraction spots indicates that there are still submicron grain sizes. A STEM-ADF image (Fig. 5C) with associated EDS maps (Fig. 5D – G) show the presence of carbon rich regions. A line scan over one of these regions (Fig. 5C, inset) shows that the region is vanadium – carbon rich. From the SAD pattern of the system after ion irradiation (Fig. 5B), the vanadium-carbon rich region may be corresponding to V_2C precipitates present in the material.

To better understand the ion irradiation response of the LSEM V44, the as-cast coarse grain V44 specimens (with grain sizes of 402±190 µm) were subjected to the same dual-beam ion irradiation conditions as the LSEM V44, but at a lower temperature of 650°C. During the in-situ temperature ramp to the elevated temperature, the coarse grain V44 began exhibiting significant microstructural changes with the formation of carbides (see Fig. 6A – 6B). The system was allowed time to briefly stabilize prior to being subjected to the dual-beam ion irradiation. The heavily defected microstructure after the ion irradiation is shown in Fig. 6C. From the SAD taken after reaching 650°C (Fig. 6B, bottom), but prior to the start of the ion irradiation, diffraction spots corresponding to vanadium carbides are observed, highlighted by orange circles. The presence of vanadium carbides is also observed by the SAD taken after the ion irradiation (Fig. 6C, bottom). Vanadium carbide formation was also observed in the LSEM V44 after heating the specimen to 700 C, but prior to beginning the ion irradiation (see Supplemental Fig. S4). The observation of vanadium carbide before and after ion irradiation

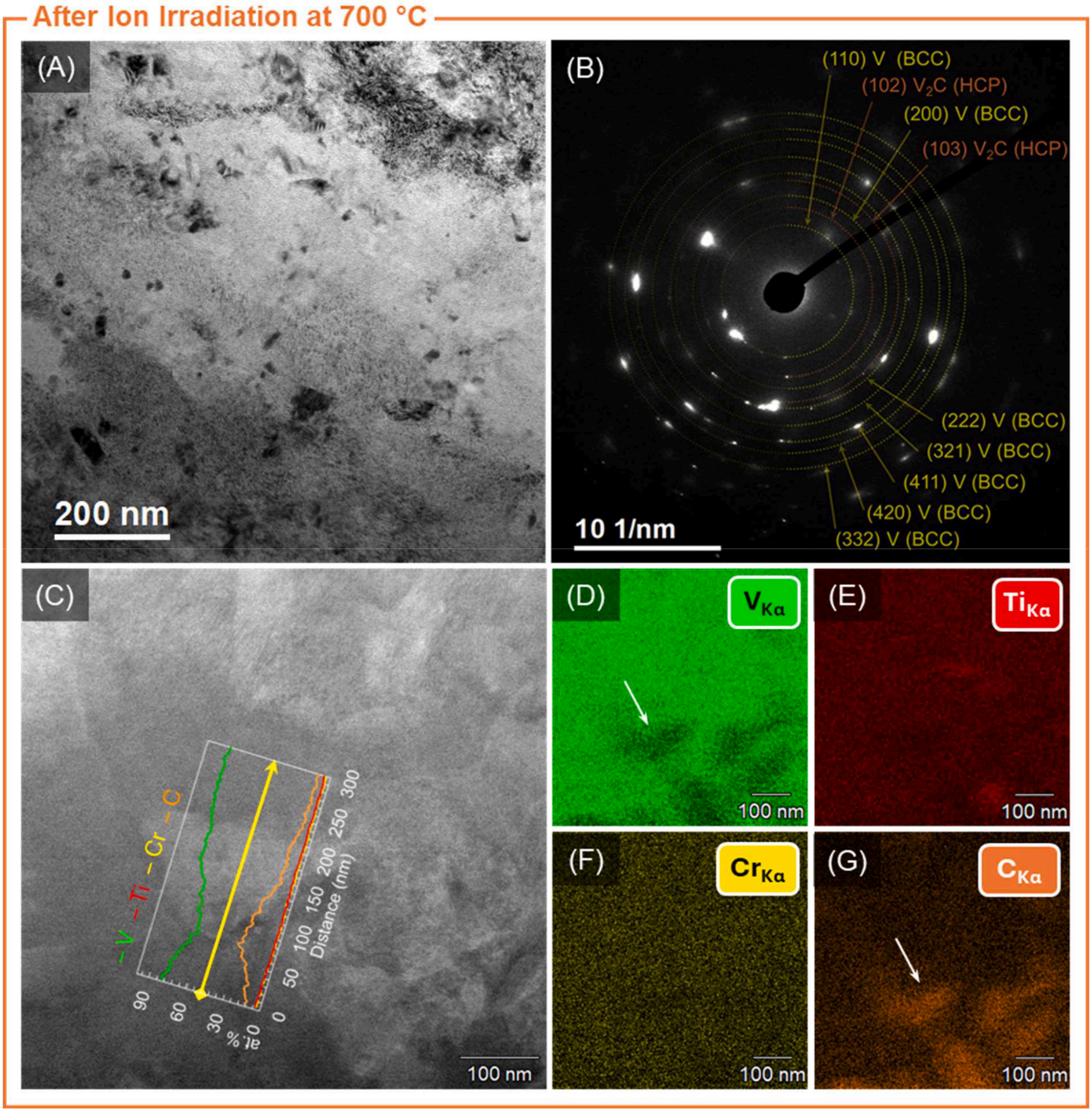

Fig. 5. Bright field TEM image with associated selected area diffraction pattern after dual-beam ion irradiation of 1 MeV Kr^{2+} and 16 KeV He^{+} at 700°C 2 ~5 dpa (A and B). STEM-ADF taken the after the dual-beam ion irradiation at 700°C (C) with associated EDS maps of V (D), Ti (E), Cr (F), and C (G). A plot of the line scan indicated by the yellow arrow in (C) is overlaid. White arrows point to a vanadium carbide phase present in the sample after the ion irradiation.

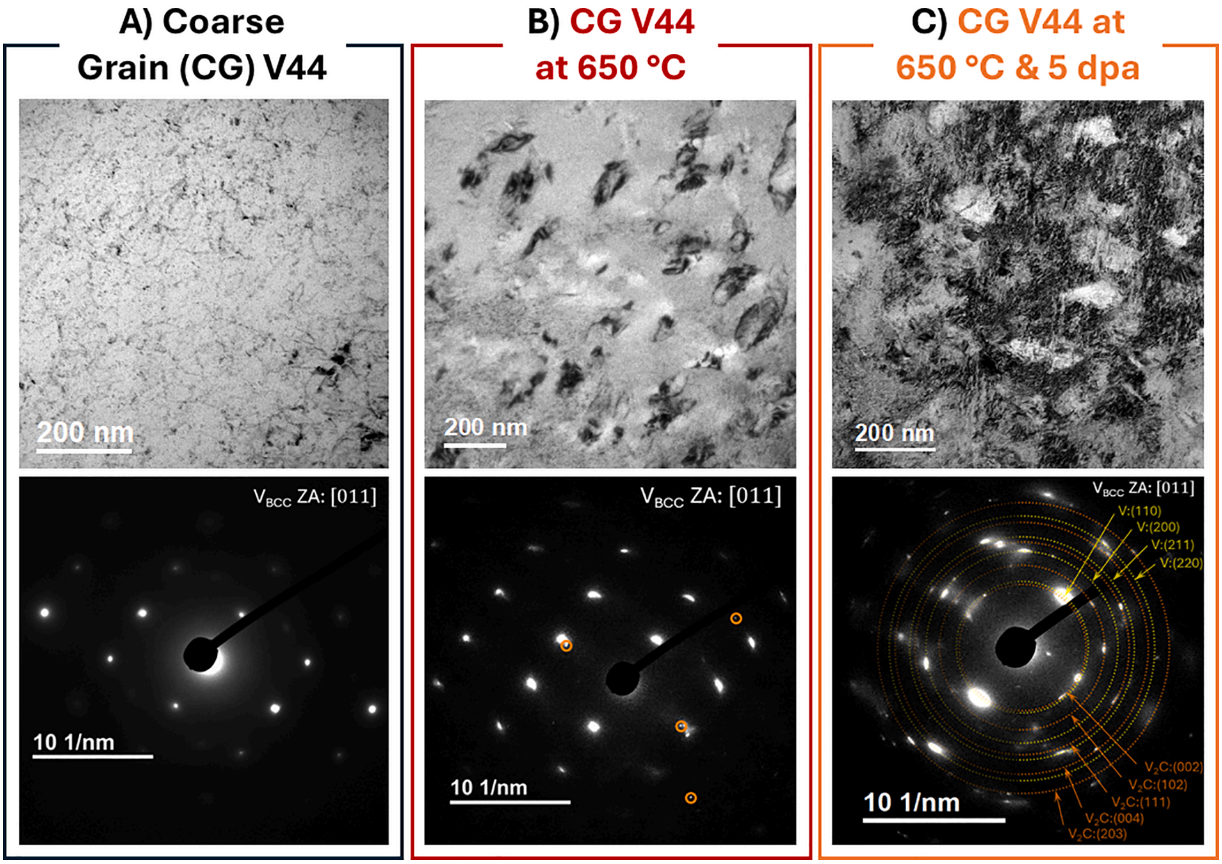

Fig. 6. Brightfield TEM image of the as-cast coarse grain V44 with associated SAD along the [011] zone axis (A). BF-TEM image of the CG V44 after heating the specimen to 650°C with its associated SAD pattern (B). Diffraction spots between and off the corners of the main vanadium diffraction spots (highlighted by the orange circles) can be observed, corresponding to vanadium carbide phases. Shown in (C) is a BF-TEM image of the CG at 650°C after dual-beam ion irradiation to 5 dpa with its associated SAD pattern. More diffraction spots can be observed, with many corresponding to V_2C.

suggests that its formation is thermally driven and not solely formed as a result of the ion irradiation.

For insight on the irradiation hardening behavior of LSEM V44, Fig. 7 compares the hardness of the coarse grain, LSEM, annealed LSEM at 700°C, and dual-beam ion irradiated LSEM at 700°C. Fig. 7A shows the instantaneous hardness calculated as a function of depth using Bruker-Hysitron's nanoDMA technique (a continuous stiffness measurement (CSM) function) applied to the loading segment. Due to the load limit of the system set up (10 mN), the hardness plots for the coarse grain and as-processed LSEM V44 do not completely stabilize. From Fig. 7A, the ion irradiated LSEM V44 exhibits a higher hardness as compared to all the conditions, with the peak hardness for the dual-beam ion irradiated LSEM V44 corresponding well with the expected combined He^+ and Kr^{2+} peak ion implantation (located ~160 nm) as simulated by SRIM

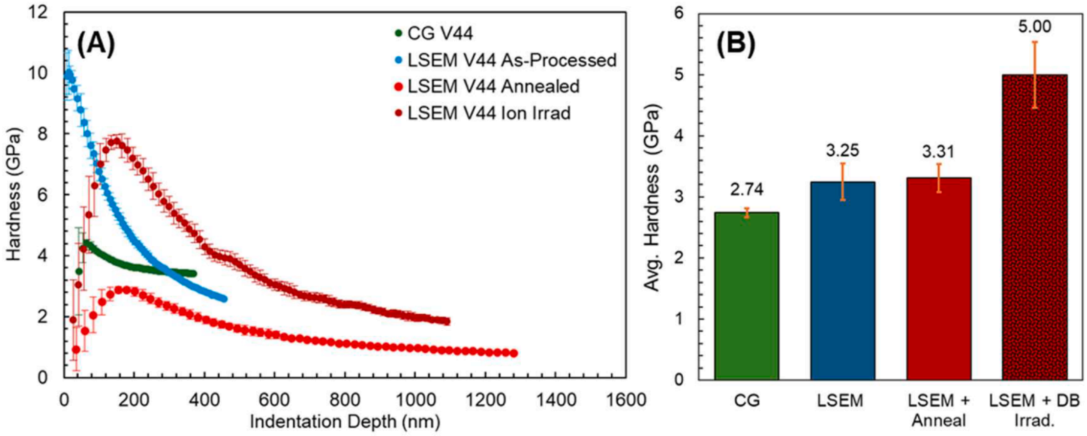

Fig. 7. Shown in (A) is a plot of the instantaneous hardness (calculated during the loading segment using nanoDMA) with respect to depth of the as-cast coarse grain, as processed LSEM, LSEM subjected to 700°C for 3948 s, and LSEM subjected to the dual-beam ion irradiation at 700°C for 3948 s. (B) shows a plot of the average hardness calculated from the unloading segment (without nanoDMA) of V44 in the as-cast coarse grain, as processed LSEM, LSEM subjected to 700°C for 3948 s, and LSEM subjected to the dual-beam ion irradiation at 700°C for 3948 s.

(Supplemental Fig. S2). Additionally, Fig. 7B shows the average hardness of the different V44 conditions, calculated from the unloading segment of the indent without nanoDMA after reaching a peak depth of 200 nm. The discrepancy between the hardness measured using quasi-static measurements (without continuous stiffness measurements) and nanoDMA measurements (with continuous stiffness measurements) may be due to the strain rate sensitivity of V44. Tensile strain rate measurements conducted at room temperature on V44 have shown increased strength at higher strain rates [33]. For the nanoDMA measurements, the oscillations were performed at 200 hz, which can be considered as a pseudo-high strain rate test. Thus, it is not surprising that the hardness is higher in the nanoDMA tests as compared to the quasi-static nanoindentation tests performed in this work.

Compared to the hardness of the as cast coarse grain V44 (2.74±0.07 GPa), the as processed LSEM specimen has a higher average hardness (3.25±0.30 GPa). The increased hardness is expected considering the large fraction of nanocrystalline and ultrafine grain sizes and boundaries. As the sample possesses multimodal grain size distribution, it is not surprising for some indents to land on larger grains that possess a response similar to the coarse grain V44. The hardness does not significantly change after annealing the specimen at 700°C for 3948 s (3.31 ±0.23 GPa).

Generally, the strength of a material can be described by the contributions stemming from its intrinsic lattice friction, the number of grain (Hall-Petch) and twin boundaries, the density of dislocation networks (Taylor strengthening), strengthening based on the system's solid solution, and strengthening from the presence of oxide, precipitates, or secondary phases [34]. When compared to the as-cast coarse grain V44, the high temperature irradiated LSEM V44 possesses a significant increase in grain boundaries, including the possibility of twin boundaries, which has been observed in other irradiated V44 work [35], leading to Hall-Petch and twin boundary strengthening. Due to the large strain extrusion process and ion irradiation, there is also a significant increase in defects and dislocations present in the material, suggesting Taylor strengthening will also play a role in enhancing its strength. Finally, from compositional and impurity characterization as well as from the identification of carbide and oxide phases from SAD, solid solution and precipitation strengthening will also contribute to strengthening the material. Thus, it is expected that the refined grained LSEM V44 possesses enhanced hardness. Future focused studies are required to isolate and determine the contributions from the variety of strengthening mechanisms involved.

The negligible change in hardness after heat treatment may be attributed to two competing mechanisms. As-processed LSEM produces a severely deformed microstructure (which can be observed by the EBSD maps shown in Fig. 1E – G). Thus, when subjected to 700°C for 3948 s, dislocations, especially near the surface, are expected to anneal out, serving to soften the material with the reduced dislocation density. From the in-situ thermal investigations, there was no significant grain growth observed at these temperatures to suggest that softening is due to a Hall-Petch relationship in which large grain sizes lead to lower hardnesses. However, as observed in the in-situ heating experiments as well as previously observed in literature, carbon impurities form vanadium carbides which serve to precipitate strengthen the system. Thus, the competition between these two mechanisms is expected to play a major role in the negligible change in hardness of the annealed LSEM specimen. When subjected to dual-beam ion irradiation at 700°C to a peak damage of ~5 dpa, the hardness increases to 5.00±0.54 GPa. Unlike in the annealed only specimen, when subjected to irradiation at elevated temperatures, the additional defect and cavity production from the ion irradiation serves as another strengthening mechanism. From SRIM calculations, the farthest that Kr^{2+} ions are expected to travel is ~600 nm. Thus, it is expected that the plastic zone (~3 times the indentation depth [36,37]) beneath the 200 nm depth indent will largely encompass the ion irradiated material. However, it should not be discounted that the damage profile is transient and not a flat profile from the surface. Future focused studies are required to isolate and determine the contributions from the variety of strengthening mechanisms involved.

4. Discussion

4.1. Microstructure and thermalstabilityof multimodalV44

As a result of LSEM, the coarse grain structure of the as-cast V44 specimen (Supplemental Fig. S1A – B) was significantly altered, forming a multimodal distribution of grains with nanocrystalline, ultrafine grained, and elongated coarse grains (Fig. 1G – I). Unlike the elongated microstructure reported in other works [22], the elongated grains here are not continuous and, instead, are mostly broken up. This type of diverse grain morphology has been previously observed [24,38,39] as a result of LSEM processing of materials susceptible to adiabatic shear banding (ASB). ASB tends to happen in materials with lower thermal conductivity and higher heat capacity like V44 alloy. Higher strain rates and temperatures typical in machining operations can promote the formation of ASBs, which lead to the heterogenous microstructure [40–42]. Strain localization within ASBs facilitates dynamic recrystallization and formation of ultrafine and equiaxed grains as observed in Fig. 1I – J [25,43,44]. Lower strains outside of ASBs result in the elongated coarse grains with subgrains (Fig. 1G – I).

The increased number of grain boundaries from nanocrystalline and ultrafine grains serve as sinks for defects, thereby improving the radiation tolerance of the material [45–48]. In addition to aiding the radiation tolerance, the multimodal grain distribution is expected to also aid in improving the mechanical performance of the system. The presence of small grains has been shown to increase the strength of a material with the boundaries acting as barriers for dislocations to pile up and requiring increasing stress to nucleate further dislocations [49,50]. Meanwhile, the presence of larger grains require more strain in order to form macrovoids for failure as well as more volume for dislocation slip to occur, thereby also improving the plasticity in the material [51–53]. Multimodal grain morphologies incorporating nanocrystalline and ultrafine grain sizes have previously been observed to lead to enhanced strength and ductility in many other material systems such as Al [54,55], Cu [56], Ti [57], Zr [52], and other compositionally complex alloys [51].

To better understand the thermal stability of V44, phase diagrams were simulated using Pandat (see Fig. 8A – B). At elevated temperatures, the general bulk phase is expected to correspond to BCC vanadium. This can be observed by the BCC vanadium spots observed in the selected area diffraction patterns for both the LSEM (see Fig. 3H, Supplemental Fig. S4B) and CG (see Fig. 6B) V44. This is also in alignment with literature of simulated ternary phase diagrams V44 at the elevated temperatures ~ 700°C [58]. The next two largest phases expected are FCC and HCP phases, though both combined may amount to ~0.005 phase fraction of the whole system. Among the more common vanadium carbides, VC possesses an FCC rock salt crystal structure and V_2C possesses a hexagonal crystal structure. From the SAD patterns observed in Fig. 3H, Fig. 5B and Fig. 6B – C, there are diffraction spots (highlighted in orange) that match well with both of these carbides and crystal structures. Thus, the phase diagrams and the experimental phases observed in the TEM match well with the observation of impurity carbide phases forming at the elevated experimental temperatures of 650°C and 700°C. The formation and presence of carbide phases may be favorable as they have been observed to improve the mechanical performance of V44 [6,59], likely serving as obstacles for dislocation motion. In terms of radiation behavior, the additional interphase boundaries between the matrix and the carbide phases is expected to serve as sinks for defects [60].

In addition to simulating phase diagrams, Monte Carlo simulations based on density functional theory (DFT) and a Cluster Expansion-Hamiltonian (CEH) were performed to simulate and visualize the atomic configuration (plotted with the open visualization tool (OVITO)) of V44 at various temperatures (Fig. 8B). These results match well with

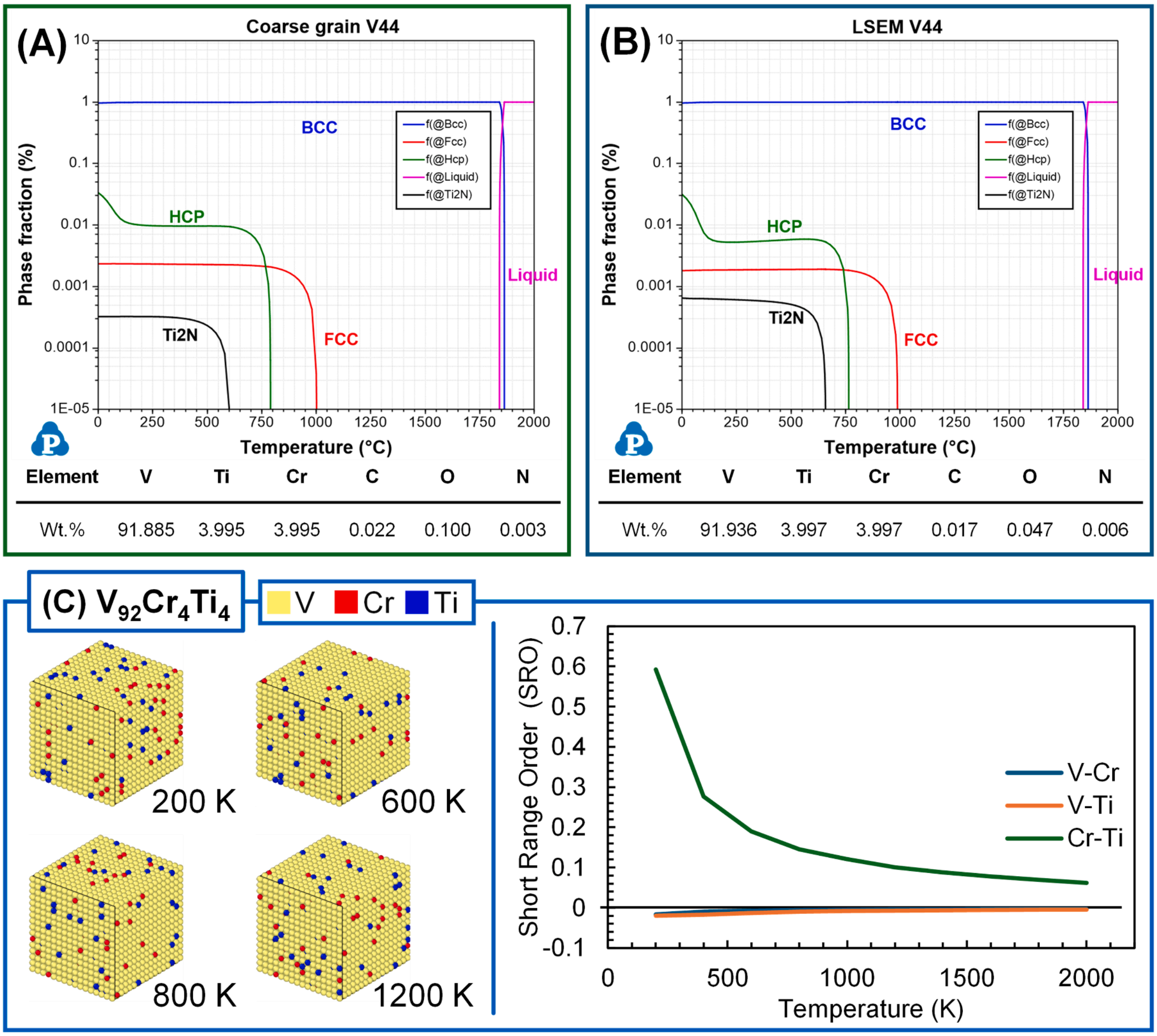

Element	V	Ti	Cr	C	O	N
Wt.%	91.885	3.995	3.995	0.022	0.100	0.003

Element	V	Ti	Cr	C	O	N
Wt.%	91.936	3.997	3.997	0.017	0.047	0.006

Fig. 8. Phase diagram simulated using Pandat of V44 as-cast (A) and after LSEM processing (B) with a table of their respective compositions underneath the phase diagram. Shown in (C) are the atomic configurations (left) from 200 K to 1200 K of V44 as well as the short-range ordering parameter with respect to temperature (right) using Monte Carlo (MC) modeling based on Density Functional Theory (DFT) and cluster expansion-Hamiltonian (CEH).

those performed by others in literature using finer temperature step sizes [61]. From the atomic configurations (Fig. 8B, left), the system appears quite homogenized with the short range ordering (SRO) parameter [62] between the V – Ti and V – Cr binaries already near zero (Fig. 8B, right). As the temperature increases to 800 K and further to 1200 K, there appears to be more intermixing between the Ti and Cr atoms, and indeed from plotting the short-range ordering parameter with respect to increasing temperature, there is less repulsion between Ti and Cr. Though, to start, the repulsive force between Ti and Cr was already low. These simulations suggest that at the elevated temperatures in the matrix and away from impurities, no compositional segregation is expected.

Several groups have investigated different processing treatments of V44 to enhance its mechanical properties, especially at elevated temperatures. Tyumentsev et al. have investigated thermomechanical treatments involving a series of homogenization, aging, hydraulic compression, and multiple rolling cycles under various conditions, determining that the combination of heterophase nanostructuring and fine grained microstructure leads to increased high temperature strengths [12,21]. Smirnov et al. also performed a series of thermomechanical treatments involving high temperature homogenization, extrusion, and multiple rolling cycles, but the final specimen was finished with vacuum annealing at different temperatures [22]. With increasing finishing annealing temperatures for 1 hour, the hardness of the specimen continuously dropped with a sharp decrease after 800°C. At the same time, significant recrystallization and grain growth was observed at 800°C. Ding et al. aged V-4Ti-4Cr at 800°C, followed by room temperature reductions to different strain levels, and finishing with by annealing the specimen at 1100°C for 1 hour [11]. This treatment led to increased strengths in both the aged and cold-rolled specimen; however, the strength appears to be unstable under ion irradiation at elevated temperatures. Chernov et al. compared RAFM steels and V-4Ti-4Cr subjected to a traditional thermal treatment involving normalization and tempering and an additional special thermal cycling treatment [20]. This treatment led to a homogeneous distribution of precipitates throughout the specimen which appeared to stably exist with the main BCC phase of the system. In all cases, elongated microstructures with large grains were observed, apart from those that were finished with a high temperature anneal above 800°C.

The work here also produced regions of elongated grain microstructure, as well as the presence of equiaxed ultrafine and nanocrystalline grains can also be observed within some of the ASB. Moreover, when exposed to the elevated temperatures of 800°C for 30 min, the refined grain microstructure remained stable with negligible grain growth as observed by the in-situ TEM heating experiments. Negligible grain growth was also observed after the dual-beam ion irradiation that was performed at 700°C for 3948 s (65 min and 48 s). At elevated temperatures, only the formation of vanadium carbide was observed, consistent with findings reported in literature on the thermal stability of vanadium and its alloys. To better understand the origin of the carbide precipitation occurring in this system, analysis of the C, O, and N impurities were performed on specimens before and after LSEM processing (see Section 2.1). It was found that after LSEM processing, the impurity concentration of O and C decreased by 0.053 wt. % and 0.005 wt. %, respectively. The reduction in impurity content as a result of mechanical deformation has been observed in stainless steels subjected to a tensile strain to failure in ultrahigh vacuum with outgassing of hydrocarbons [63,64]. However, in the cited literature, outgassing of hydrocarbons is attributed to hydrocarbons adsorbed to the surface of the steel, which was released during the tensile strain and subsequent failure. Here, the C – O – N were present in the as-cast specimen and later decreased after the LSEM processing. It is suspected that for this system during the LSEM process, oxygen in solution of the as-cast V44, may be rapidly migrating to the newly formed grain boundaries prior to being released with the local elevated temperature. Thus, compared to other multi-step thermomechanical treatments, LSEM serves as a single step thermomechanical process to refine the grain microstructure of V44 with nanocrystalline and ultrafine grains, possessing comparable thermal stability as the unprocessed coarse grain V44.

4.2. Ion irradiation response of multimodal V44 as compared to coarse grain and literature

In this work, multimodal V44 subjected to ion irradiation possesses notable irradiation tolerance with the presence of small cavities that are well-dispersed throughout the grain matrix. The preferential clustering of cavities at the grain boundaries was also observed, with minor observable coalescence of cavities at the boundaries given the temperatures and dose that the specimen was exposed to. The formation of small precipitates can be observed during the ion irradiation (Supplemental Video S1), however, compared to the coarse grain (CG) ion irradiation (Supplemental Video S2), the formation of these precipitates was not as prolific.

The observation of vanadium carbides after the ion irradiation at 700°C, is expected as they have been previously observed in literature to be stable at similar conditions [59]. Their formation was also observed in the isolated *in-situ* TEM heating investigation discussed above, as well as in literature after elevated temperature ion irradiation, aging, and annealing investigations [9,11,21,65]. The elongated and plate-like shape, as well as the sizes are similar to those reported for vanadium and other alloys [66]. Since their presence was observed prior to the onset of the ion irradiation for both the LSEM (Supplemental Fig. S4) as well as for the coarse grain (Fig. 6B) V44, the formation of vanadium carbides is suspected to be thermally driven, and not a result of ion irradiation. After being exposed to ion irradiation at elevated temperatures, the vanadium carbides remain stable and do not show signs of dissolution or a diffusion to form other carbides.

The overall areal cavity density and equivalent area diameter behavior of the multimodal V44 specimen with respect to dose is shown in Fig. 9. With increasing dose, the areal cavity density increases to a value of 0.024±0.007 cavities/nm^2 at 5 dpa. In terms of the equivalent area diameter, there was an overall increase in the size to 3 dpa, peaking at 3.7±0.6 nm, followed by a drop in size to 3.3±0.5 nm at 5 dpa. The calculated swelling at 5 dpa for the multimodal V44 based on the average number of cavities, their average size, and the thickness measurement determined by EFTEM is 0.236 %. To better qualify these results, the same dual-beam ion irradiation of 1 MeV Kr^{2+} and 16 KeV He^{+} was performed on coarse grain V44 (see Fig. 6), though the irradiation occurred at 650°C, as opposed to the 700°C which was used for the LSEM V44 specimen. From Fig. 6B, the formation of vanadium carbides can be observed from both the BF-TEM image as well as the associated SAD pattern of the CG V44, with orange circles highlighting the additional diffraction spots corresponding to vanadium carbides. To minimize the further formation of vanadium carbide, the ion irradiation was conducted at 650°C. The final microstructure after the elevated temperature dual-beam ion irradiation is shown in Fig. 6C. In multiple regions, there are heavily defected regions throughout the CG V44 grain matrix. The presence of vanadium carbides persists, as evidenced by the diffraction pattern. There is also the broadening of the diffraction spots which have been previously observed in ion irradiation to be an indicator of a damaged and defected lattice structure. Cavity analysis of the CG V44 after the dual-beam ion irradiation at 650°C, reveal an areal cavity density of 0.020±0.001 cavities/nm^2 with an equivalent area diameter of 4.3±0.7 nm.

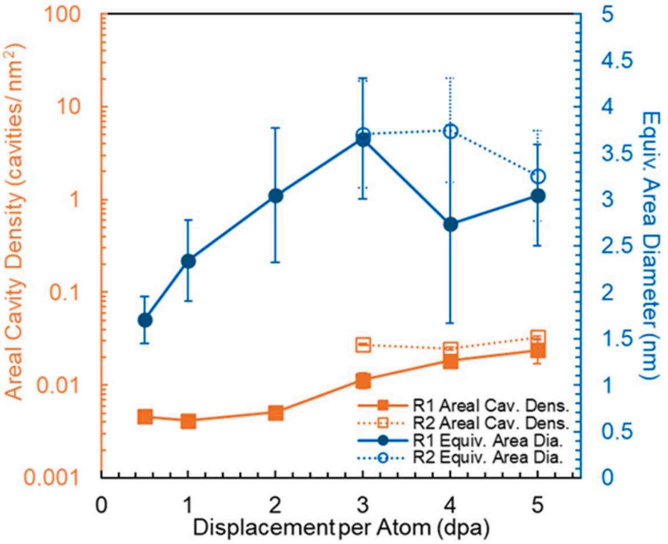

Fig. 9. Plot of the cavity analysis in terms of areal cavity density and equivalent area diameter with respect to dose (dpa) (A). From 3 dpa to 5 dpa, a second region began to be tracked (see Fig. 4G – I, Region 2).

Compared to the coarse grain, the average equivalent area diameter of cavities in the LSEM V44 is lower, however the standard deviations between the two overlaps, suggesting a small improvement in ion irradiation tolerance. With respect to the areal cavity diameter, the LSEM possesses a slightly higher areal density as compared to the CG V44, however the standard deviations also overlap. It is likely that small cavities coalesced in the CG V44, leading to a lower overall areal density of cavities as compared to the LSEM specimen. As mentioned previously, irradiation studies of grain refined materials have generally observed improvements in irradiation tolerance, generally attributed to the increased number of grain boundaries serving as efficient interstitial sinks which annihilate with vacancies near the grain boundary [67]. However, despite the significant increase in grain boundaries and interfaces in this work, the improvement in ion irradiation is negligible. This may be suggesting that the grain matrix plays a more dominant role as compared to the grain boundaries in V44 systems. This behavior has been previously observed in other alloys, notably in compositionally complex alloys (CCA) [68]. For nanocrystalline W-Ta-Cr-V, the rough energy landscape and high migration energy barrier of the grain matrix impeded the migration of He vacancy complexes to the grain boundaries, thereby slowing their coalescence at the grain boundary. A similar response can be observed in the LSEM V-4Cr-4Ti, though the onset of clustering can be observed after 3 dpa of the dual-beam ion irradiation. This is expected considering V44 is not as compositionally complex as the W-Ta-Cr-V system, meaning the migration energy barrier for the He vacancy complex may not be as high. Future simulations and calculations on the formation and migration energy of He vacancy complexes are required to better understand and validate the behavior observed in this work.

Regarding the precipitates observed in Fig. 6B – C, it is reasonable to assume from the SAD that some correspond to vanadium carbides, with their sizes being ~200 nm; this is larger than those observed in the LSEM V44 which are ~100 nm in terms of the longest diameter. Due to the sever plastic deformation, the LSEM V44 is expected to possess a larger number of dislocation cores as compared to the CG V44. Between the carbon – dislocation interaction, there can be attractive forces. Thus, if there are a wider spread and a larger number of dislocation cores in the specimen due to the LSEM process, this may lead to a homogenous distribution of carbon within the system. With the complex strain fields associated with the large number of dislocations and grain boundaries, this may serve to slow the kinetics for the formation and growth of these precipitates leading to the observed smaller carbide sizes in the LSEM V44. From the TEM images and *in-situ* TEM videos (Supplemental Video S1 and S2) there is also a noticeable difference in the presence of point defects and damage evolution which were prolific and longstanding in the coarse grain V44 as compared to the multimodal LSEM V44. These all suggest improvements in the ion irradiation behavior as a result of the LSEM process in V44.

When comparing the LSEM ion irradiation cavity numbers and sizes with literature (see Table 2), the observed values are higher. However, when comparing the size of cavities, the size reported here are significantly smaller with an upper limit of 3.3±0.5 nm. When exposed to 550 KeV Fe^{+} ion irradiation to 20 dpa at 500°C, cavities were observed to be 11.1±3.3 nm at the peak dose [11]. Others have irradiated V44 with 2 MeV He^{2+} ions to 0.5 dpa at both 500°C and 700°C, observing cuboidal cavities at 700°C that are 13.9±3.5 nm in size [73]. The values here are lower despite the higher dose (5 dpa) when compared to those reported by Fukumoto et al., who observed 0.4±0.03 % swelling at 500°C and 3.3 ±1.2 % swelling at 700°C for with 2 MeV He^{2+} ions to 0.5 dpa [73]. Luo et. al. reported cavity sizes of 3.1±0.4 nm and swelling of 0.02 % as a result of 2.5 MeV Fe^{2+} at 550°C to a peak of 35 dpa [71]. In terms of equivalent area diameter, the diameter of the multimodal V44 is observed to begin to stabilize at a size similar to that observed by Luo et al. The swelling of the multimodal LSEM V44 (0.236 %) and number of cavities (0.024±0.007 cavities/nm^{2}) is comparatively higher, though this discrepancy in number of cavities and presence of helium is attributed to the dual-beam ion irradiation of 1 MeV Kr^{2+} and 16 KeV He^{+} ion performed at 700°C in this work.

Nanoindentation has been widely used to gain insight into the mechanical properties of V44, especially after irradiation. A few of these have been summarized in Table 2. Compared to most of the unirradiated V44 systems listed in the table, the LSEM V44 discussed in this work possesses a higher nanoindentation hardness, with the exception of Zhang et al. who reported a comparable hardness of 3.68±0.30 [69]. The comparable hardness observed by Zhang et al. may have been attributed to the presence of Ti-rich precipitates at the grain boundaries, which were not observed in the as-processed LSEM V44. The ion irradiated LSEM V44 performs comparably with most other V44 studied in literature, with comparable irradiation hardening as Zhang et al [69]. The irradiation hardening is not as high as what was observed by Luo et al. who reported a hardness of 9.7 GPa, though in that work the sample was irradiated to a much higher dose of 35 dpa [71].

It should be noted that many of the nanoindentation hardness values reported in literature were determined using continuous stiffness measurements (CSM) (or something similar) to plot H^2 versus $1/h$, where H is the instantaneous hardness at the respective depth, h, using the Nix-Gao model [74]. From this plot, a least square fit can be used to find the bulk, equivalent hardness H_0. The Nix-Gao model is often used as a technique for discerning and isolating indentation size effects and changes in the hardening slope of an indent due to the presence of an irradiation layer or different material near the surface of a material. However, Nix-Gao originally formulated the model based on the geometrically necessary dislocations present in single crystal or large grained systems. Similarly, many of the nanoindentation performed on irradiated V44 in literature (see Table 2) were performed on coarse grain specimens. With the Nix-Gao model, it becomes difficult to directly correlate changes in the hardening to a specific feature when there are multiple mechanisms (such as grain boundaries, precipitates, etc.) that may be observed as a function of the depth. For a multimodal grained specimen with a large fraction of nanocrystalline and ultrafine grains, multiple changes in the hardening slope can be observed in the

Table 2
Summary of Ion Irradiation, Nanoindentation Response of V-4Cr-4Ti.

Description	Microstructure/Grain Size	Irradiation Conditions	Irradiation Temperature	Peak dpa	Ion Irradiation Response	Hardness (GPa) Before Irradiation Conducted at RT	Hardness (GPa) After Irradiation Conducted at RT	Ref.
V-4Cr-4Ti (LSEM)	Multimodal with nanocrystalline and ultrafine grained (~45 %[*]), and coarse grains (~55 %[*])	16 KeV He^{+} and 1 MeV Kr^{2+}	700°C	~5	Cavity Equiv. Area Dia: 3.3±0.5 nm Swelling: 0.236 %	3.25±0.30	5.00±0.54	This Work
V-4Cr-4Ti (CG-Arc Cast)	402±190 µm	16 KeV He^{+} and 1 MeV Kr^{2+}	650°C	~5	Cavity Equiv. Area Dia: 4.3±0.7 nm	2.74±0.07	-	This Work
V-4Cr-4Ti (Zhang et al.)	~20 µm	30 KeV H^{+} and 50 KeV He^{+}	450°C	0.18	-	3.68±0.30	5.05±0.37	[69]
V-4Cr-4Ti (Miyazawa et al.)	~20 – 30 µm	2.4 MeV Cu^{2+}	200°C	7.6	-	1.6	3.15	[70]
V-4Cr-4Ti (Luo et al.)	424 ± 124 µm	2.5 MeV Fe^{2+}	550°C	35	Cavity Dia: 3.1±0.4 nm Swelling: 0.02 %	2.5	9.7	[71]
V-4Cr-4Ti (Fukumoto et al.)	~20 – 30 µm	2 MeV He^{2+}	500°C	3.6	-	1.4	1.9	[72]
V-4Cr-4Ti (Ding et al.)	Coarse grains >10 µm	550 KeV Fe^{+}	500°C	20	Cavity Dia: 11.1 ±3.3 nm Swelling: -	-	-	[11]
V-4Cr-4Ti (Fukumoto et al.)	~20 – 30 µm	2 MeV He^{2+}	500°C	0.5	Cavity Dia: -Swelling: 0.4±0.03 %	-	-	[73]
V-4Cr-4Ti (Fukumoto et al.)	~20 – 30 µm	2 MeV He^{2+}	700°C	0.5	Cavity Dia.:13.9 ±3.5 nm Swelling: 3.3±1.2 %	-	-	[73]

[*] Percentage represents the weighted area fraction of grains

as-processed specimen, making it challenging to interpret an appropriate bulk hardness (H_0) from the as-processed specimen. The hardening curve from the loading segment is more complex after annealing the specimen at 700°C, attributed to the formation of carbides. Moreover, ion irradiation adds another level of complexity in the interpretation of the hardening slope. As these factors should not be discounted, the values reported in Fig. 7B serve as a simplified result, encompassing all these features. The hardness values in Fig. 7B uses a simple load-unload indentation (without CSM), with the hardness, H, being calculated from the load at 95 % of the unloading curve and a contact area determined by an Oliver-Pharr fit [75]. Although the indents performed in this study targeted a final depth of 200 nm, the total plastic zone and response of the indent will also incorporate part of the unirradiated LSEM V44 underneath the ion irradiation damage zone. This is expected to underestimate the real ion irradiation hardening observed between the annealed only LSEM V44 and the dual-beam ion irradiated at 700°C LSEM V44. Further controlled, targeted investigations are required to more accurately probe the hardening response associated with only the ion irradiation damage layer, as well as evaluate other mechanical properties (e.g. tensile, compression, and Vicker's Hardness) of LSEM V44 under extreme conditions.

5. Summary

This work showcases homogeneous V-4Cr-4Ti synthesized using arc melting which was successfully processed by large strain extrusion machining to produce a modified elongated multimodal microstructure composed of a majority of nanocrystalline and ultrafine grains. LSEM processing produces a severely plastically deformed microstructure with the presence of elongated grains and adiabatic shear bands. In terms of thermal stability, vanadium carbides began forming in the multimodal V44 after reaching 600°C. Little grain growth was observed after reaching 800°C and holding the system at an elevated temperature for 30 min. After being exposed to dual-beam ion irradiation at 700°C, cavities can be observed throughout the system, though there is preferential clustering at the grain boundaries. Despite the clustering at the grain boundaries, the cavities exhibit little coalescence when exposed to ~5 dpa at 700°C. There was a slight increase in the areal cavity density of cavities to ~ 5 dpa and the equivalent area diameter of cavities appear to have stabilized around 3 nm. Compared to the as-cast and unprocessed coarse grain V44 shown in this work, a lower number of other phases and precipitates were observed to have formed during the dual beam ion irradiation. In addition, a larger local area fraction of point defects from the ion irradiation remained in the CG V44 as compared to the LSEM V44 as observed from the *in-situ* ion irradiation videos. Nanoindentation reveals a ~50 % increase in the hardness of the LSEM V44 after the dual-beam ion irradiation at 700°C. Further investigations are suggested to further quantify the mechanical capabilities and irradiation hardening mechanisms of LSEM V44. Ultimately, the LSEM V44 possesses similar ion irradiation response as what has been previously observed in literature. What is key to note is the grain stability of the LSEM V44 after ion irradiation. Negligible grain growth was observed at 700°C, and despite the smaller grain size, the formation of precipitates and phases were slower than what was observed in the CG V44 which was ion irradiated at the lower temperature of 650°C. Future work remains to understand the mechanical properties of multimodal V44 processed by LSEM and when subjected to extreme conditions such as temperature and irradiation. In addition, computational modeling and simulations of the formation and migration energies of defects will help to elucidate the underlying mechanisms of the ion irradiation response in vanadium-based alloys.

Data availability

All data needed to evaluate the conclusions in the paper are present in the paper and/or Supplementary Materials. Additional data related to this paper may be made available on request.

CRediT authorship contribution statement

Skye Supakul: Writing – review & editing, Writing – original draft, Visualization, Validation, Methodology, Investigation, Formal analysis, Data curation. **Eda Aydogan:** Writing – review & editing, Validation, Supervision, Investigation. **Mert Efe:** Writing – review & editing, Writing – original draft, Resources, Methodology. **Matthew Vigil:** Writing – review & editing, Writing – original draft, Resources, Methodology. **Bochuan Sun:** Writing – review & editing, Writing – original draft, Investigation, Formal analysis. **Ishtiaque Robin:** Writing – review & editing, Validation, Investigation. **Kayla Yano:** Writing – review & editing, Investigation, Formal analysis. **Wei-Ying Chen:** Writing – review & editing, Resources, Investigation. **Damian Sobieraj:** Writing – review & editing, Resources. **Jan S. Wróbel:** Writing – review & editing, Resources. **Duc Nguyen-Manh:** Writing – review & editing, Resources. **Enrique Martinez:** Writing – review & editing, Validation, Methodology, Conceptualization. **Dan Thoma:** Writing – review & editing, Validation, Resources, Methodology, Conceptualization. **Stuart Maloy:** Writing – review & editing, Supervision, Resources, Project administration, Funding acquisition. **Osman El-Atwani:** Writing – review & editing, Visualization, Validation, Supervision, Resources, Project administration, Methodology, Funding acquisition, Data curation, Conceptualization.

Declaration of competing interest

The authors declare that they have no known competing financial interests or personal relationships that could have appeared to influence the work reported in this paper.

Acknowledgments

This work was supported by the U.S. Department of Energy, Advanced Research Projects Agency-Energy under contract DE-FOA-0003240, project number 84026A. This work was also supported by an Energy & Environment Directorate Mission Seed Laboratory Directed Research and Development (LDRD) project at Pacific Northwest National Laboratory. A portion of this research was performed on project award 61570 from the Environmental Molecular Sciences Laboratory, a DOE Office of Science User Facility sponsored by the Biological and Environmental Research program under Contract No. DE-AC05-76RL01830. This work was supported by the U.S. Department of Energy, Office of Nuclear Energy under DOE Idaho Operations Office Contract DE-AC07-05ID14517 as part of Nuclear Science User Facilities award #23–4744. The work at UKAEA was partially supported by the Broader Approach Phase II agreement under the PA of IFERC2-T2PA02. Views and opinions expressed were however those of the author(s) only and do not necessarily reflect those of the European Union or the European Commission. Neither the European Union nor the European Commission can be held responsible for them. D.N.M. also acknowledged funding by the EPSRC Energy Programme (grant number EP/W006839/1). This work was also completed with the help of Tim McAllister and Michael Blazon for their help in the LSEM processing and sample preparation, respectively.

Supplementary materials

Supplementary material associated with this article can be found, in the online version, at doi:10.1016/j.actamat.2026.121977.

References

[1] G.J. Butterworth, Low activation structural materials for fusion, Fusion Eng. Des. 11 (1) (1989) 231–244.

[2] E.E. Bloom, R.W. Conn, J.W. Davis, R.E. Gold, R. Little, K.R. Schultz, D.L. Smith, F. W. Wiffen, Low activation materials for fusion applications, J. Nucl. Mater. 122 (1) (1984) 17–26.

[3] R.H. Jones, H.L. Heinisch, K.A. McCarthy, Low activation materials, J. Nucl. Mater. 271-272 (1999) 518–525.

[4] T. Muroga, J.M. Chen, V.M. Chernov, R.J. Kurtz, M.L. Flem, Present status of vanadium alloys for fusion applications, J. Nucl. Mater. 455 (1) (2014) 263–268.

[5] S.J. Zinkle, H. Matsui, D.L. Smith, A.F. Rowcliffe, E. van Osch, K. Abe, V. A. Kazakov, Research and development on vanadium alloys for fusion applications, J. Nucl. Mater. 258-263 (1998) 205–214.

[6] T. Muroga, P.F. Zheng, Y. Yang, History, present status, and future directions of vanadium alloys for fusion reactors, Curr. Opin. Solid. State Mater. Sci. 36 (2025) 101224.

[7] D.L. Smith, B.A. Loomis, D.R. Diercks, Vanadium-base alloys for fusion reactor applications — a review, J. Nucl. Mater. 135 (2) (1985) 125–139.

[8] H.M. Chung, D.L. Smith, Tensile and impact properties of vanadium-base alloys irradiated at <430°C1Work supported by the office of fusion energy, US department of energy, under contract W-31-109-eng-38.1, J. Nucl. Mater. 258-263 (1998) 1442–1450.

[9] T. Muroga, T. Nagasaka, K. Abe, V.M. Chernov, H. Matsui, D.L. Smith, Z.Y. Xu, S. J. Zinkle, Vanadium alloys – overview and recent results, J. Nucl. Mater. 307-311 (2002) 547–554.

[10] D.R. Diercks, B.A. Loomis, Alloying and impurity effects in vanadium-base alloys, J. Nucl. Mater. 141-143 (1986) 1117–1124.

[11] J. Ding, S. Yang, B. Zhu, Q. Li, Y. Long, F. Wan, Influence of high-temperature ion irradiation on microstructures of the deformed and heat-treated V-4Cr-4Ti alloy, Fusion Eng. Des. 125 (2017) 407–414.

[12] A.N. Tyumentsev, I.A. Ditenberg, K.V. Grinyaev, V.M. Chernov, M.M. Potapenko, Multi-directional forge molding as a promising method of enhancement of mechanical properties of V–4Ti–4Cr alloys, J. Nucl. Mater. 413 (2) (2011) 103–106.

[13] H. Watanabe, T. Muroga, T. Nagasaka, Effects of irradiation environment on V–4Cr–4Ti alloys, Plasma Fusion Res. 12 (2017), 2405011-2405011.

[14] R.W. Conn, Report of the DOE panel on low activation materials for fusion applications, United States, 1983.

[15] C. Zhang, P. Zhang, R. Li, J. Zhao, C. Dong, Stability and migration of vacancy in V–4Cr–4Ti alloy: effects of Al, Si, Y trace elements, J. Nucl. Mater. 442 (1) (2013) 370–376.

[16] A. Impagnatiello, T. Toyama, E. Jimenez-Melero, Ti-rich precipitate evolution in vanadium-based alloys during annealing above 400°C, J. Nucl. Mater. 485 (2017) 122–128.

[17] T. Furuno, H. Kurishita, T. Nagasaka, A. Nishimura, T. Muroga, T. Sakamoto, S. Kobayashi, K. Nakai, S. Matsuo, H. Arakawa, Effects of grain size on high temperature creep of fine grained, solution and dispersion hardened V–1.6Y–8W–0.8TiC, J. Nucl. Mater. 417 (1) (2011) 299–302.

[18] P.F. Zheng, J.M. Chen, T. Nagasaka, T. Muroga, J.J. Zhao, Z.Y. Xu, C.H. Li, H.Y. Fu, H. Chen, X.R. Duan, Effects of dispersion particle agents on the hardening of V–4Cr–4Ti alloys, J. Nucl. Mater. 455 (1) (2014) 669–675.

[19] T. Nagasaka, T. Muroga, M. Imamura, S. Tomiyama, M. Sakata, Fabrication of high-purity V-4CR-4TI low activation alloy products, Fusion Technol. 39 (2P2) (2001) 659–663.

[20] V.M. Chernov, M.V. Leonteva-Smirnova, M.M. Potapenko, N.I. Budylkin, Y. N. Devyatko, A.G. Ioltoukhovskiy, E.G. Mironova, A.K. Shikov, A.B. Sivak, G. N. Yermolaev, A.N. Kalashnikov, B.V. Kuteev, A.I. Blokhin, N.I. Loginov, V. A. Romanov, V.A. Belyakov, I.R. Kirillov, T.M. Bulanova, V.N. Golovanov, V. K. Shamardin, Y.S. Strebkov, A.N. Tyumentsev, B.K. Kardashev, O.V. Mishin, B. A. Vasiliev, Structural materials for fusion power reactors—the RF R&D activities, Nucl. Fusion 47 (8) (2007) 839.

[21] A.N. Tyumentsev, I.A. Ditenberg, K.V. Grinyaev, I.V. Smirnov, Y.P. Pinzhin, A. D. Korotaev, V.M. Chernov, M.M. Potapenko, M.V. Kravtsova, K.A. Moroz, N. A. Degtyarev, Microstructure and mechanical properties of low-activation V–4Ti–4Cr–(C, O, N) Vanadium alloys depending on conditions of their technological and thermomechanical treatment, Phys. At. Nucl. 86 (7) (2023) 1564–1576.

[22] I.V. Smirnov, I.A. Ditenberg, K.V. Grinyaev, A.N. Tyumentsev, Y.P. Pinzhin, D. A. Osipov, Influence of the annealing temperature on the grain structure of V–4Ti–4Cr alloy after thermomechanical treatment with rolling, Russ. Phys. J. 65 (12) (2023) 2231–2237.

[23] O. El-Atwani, J. Hinks, G. Greaves, S. Gonderman, T. Qiu, M. Efe, J.P. Allain, In-situ TEM observation of the response of ultrafine-and nanocrystalline-grained tungsten to extreme irradiation environments, Sci. Rep. 4 (2014) 4716.

[24] M. Efe, O. El-Atwani, Y. Guo, D.R. Klenosky, Microstructure refinement of tungsten by surface deformation for irradiation damage resistance, Scr. Mater. 70 (2014) 31–34.

[25] M. Efe, W. Moscoso, K.P. Trumble, W. Dale Compton, S. Chandrasekar, Mechanics of large strain extrusion machining and application to deformation processing of magnesium alloys, Acta Mater. 60 (5) (2012) 2031–2042.

[26] T. Malis, S.C. Cheng, R.F. Egerton, EELS log-ratio technique for specimen-thickness measurement in the TEM, J. Electron. Microsc. Tech. 8 (2) (1988) 193–200.

[27] M. Li, W.-Y. Chen, P.M. Baldo, In situ transmission electron microscopy with dual ion beam irradiation and implantation, Mater. Charact. 173 (9) (2021) 110905.

[28] R.E. Stoller, M.B. Toloczko, G.S. Was, A.G. Certain, S. Dwaraknath, F.A. Garner, On the use of SRIM for computing radiation damage exposure, Nucl. Instrum. Methods Phys. Res. B: Beam Interact. Mater. At. 310 (2013) 75–80.

[29] O. El-Atwani, H. Vo, N. Krienke, E. Martinez, J.K. Baldwin, W.-Y. Chen, M. Li, S. Fensin, Comparison of dislocation loop formation resistance in nanocrystalline and coarse-grained refractory high entropy alloys, High Entropy Alloys Mater 1 (2) (2023) 260–265.

[30] C.L. Woodcock, D.F. Bahr, Plastic zone evolution around small scale indentations, Scr. Mater. 43 (9) (2000) 783–788.

[31] X. Li, H. Zhang, S. Lu, W. Li, J. Zhao, B. Johansson, L. Vitos, Elastic properties of vanadium-based alloys from first-principles theory, Phys. Rev. B 86 (1) (2012) 014105.

[32] J.V. Haag, M.J. Olszta, D.J. Edwards, W. Jiang, W. Setyawan, Visualization of three-dimensional helium cavity distribution in an ion-irradiated tungsten heavy alloy for nuclear fusion materials, Microsc. Microanal. 29 (Supplement_1) (2023), 1565-1565.

[33] A.F. Rowcliffe, S.J. Zinkle, D.T. Hoelzer, Effect of strain rate on the tensile properties of unirradiated and irradiated V–4Cr–4Ti, J. Nucl. Mater. 283-287 (2000) 508–512.

[34] T.E.J. Edwards, T. Xie, N. Maria della Ventura, D. Casari, C. Guerra, E. Huszár, X. Maeder, J.J. Schwiedrzik, I. Utke, L. Pethö, J. Michler, On the thinnest Al2O3 interlayers in Al-based nanolaminates to enhance strength, and the role of constraint, Acta Mater. 240 (2022) 118345.

[35] J. Ding, S. Yang, B. Zhu, H. Liu, G. Liu, L. Zhou, Q. Zhan, F. Wan, Twins induced by high-temperature ion irradiation in body-centered cubic V-4Cr-4Ti alloy, Scr. Mater. 162 (2019) 377–381.

[36] N.A. Sakharova, J.V. Fernandes, J.M. Antunes, M.C. Oliveira, Comparison between Berkovich, Vickers and conical indentation tests: a three-dimensional numerical simulation study, Int. J. Solids. Struct. 46 (5) (2009) 1095–1104.

[37] O. Iracheta, C.J. Bennett, W. Sun, The influence of the indentation size in relation to the size of the microstructure of three polycrystalline materials indented with a Berkovich indenter, Mater. Sci. Eng. A 706 (2017) 330–341.

[38] Q. Wang, R.M. Shankar, Z. Liu, Y. Cheng, Crystallographic texture evolutions of Ti-6Al-4V chip foils in relation to strain path and high strain rate arising from large strain extrusion machining process, J. Mater. Process. Technol. 305 (2022) 117588.

[39] S.L. Cai, L.H. Dai, Suppression of repeated adiabatic shear banding by dynamic large strain extrusion machining, J. Mech. Phys. Solids. 73 (2014) 84–102.

[40] C.Z. Duan, L.C. Zhang, Adiabatic shear banding in AISI 1045 steel during high speed machining: mechanisms of microstructural evolution, Mater Sci Eng: A 532 (2012) 111–119.

[41] C.Z. Duan, Y.J. Cai, M.J. Wang, G.H. Li, Microstructural study of adiabatic shear bands formed in serrated chips during high-speed machining of hardened steel, J. Mater. Sci. 44 (3) (2009) 897–902.

[42] Z.P. Wan, Y.E. Zhu, H.W. Liu, Y. Tang, Microstructure evolution of adiabatic shear bands and mechanisms of saw-tooth chip formation in machining Ti6Al4V, Mater. Sci. Eng.: A 531 (2012) 155–163.

[43] H. Luo, W. Zeng, H. Chen, B. Wang, B. Xu, Effect of microstructure on plastic deformation near the ASB, microcrack nucleation behaviour and dynamic mechanical properties of TC21 alloy under dynamic compression, Mater Sci Eng: A 935 (2025) 148362.

[44] Q. Zhang, X. Liu, J. Liu, M. Zhang, W. Guo, J. Hu, X. Xu, J. Lv, H. Lai, ASB-based microcrack initiation mechanisms in railway steel under high strain rate impact, Eng. Fail. Anal. 186 (2026) 110485.

[45] N. Nita, R. Schaeublin, M. Victoria, Impact of irradiation on the microstructure of nanocrystalline materials, J. Nucl. Mater. 329-333 (2004) 953–957.

[46] J.W. Yeh, S.K. Chen, S.J. Lin, J.Y. Gan, T.S. Chin, T.T. Shun, C.H. Tsau, S.Y. Chang, Nanostructured high-entropy alloys with multiple principal elements: novel alloy design concepts and outcomes, Adv. Eng. Mater. 6 (5) (2004) 299–303.

[47] O. El-Atwani, J. Hinks, G. Greaves, J. Allain, S. Maloy, Grain size threshold for enhanced irradiation resistance in nanocrystalline and ultrafine tungsten, Mater. Res. Lett. (2017) 1–7.

[48] Y. Zhang, M.A. Tunes, M.L. Crespillo, F. Zhang, W.L. Boldman, P.D. Rack, L. Jiang, C. Xu, G. Greaves, S.E. Donnelly, L. Wang, W.J. Weber, Thermal stability and irradiation response of nanocrystalline CoCrCuFeNi high-entropy alloy, Nanotechnology. 30 (29) (2019) 294004.

[49] Y. Zou, H. Ma, R. Spolenak, Ultrastrong ductile and stable high-entropy alloys at small scales, Nat. Commun. 6 (1) (2015) 7748.

[50] Y.M. Wang, T. Voisin, J.T. McKeown, J. Ye, N.P. Calta, Z. Li, Z. Zeng, Y. Zhang, W. Chen, T.T. Roehling, Additively manufactured hierarchical stainless steels with high strength and ductility, Nat. Mater. 17 (1) (2018) 63–71.

[51] B. Schuh, R. Pippan, A. Hohenwarter, Tailoring bimodal grain size structures in nanocrystalline compositionally complex alloys to improve ductility, Mater. Sci. Eng: A 748 (2019) 379–385.

[52] D. Guo, M. Li, Y. Shi, Z. Zhang, H. Zhang, X. Liu, B. Wei, X. Zhang, High strength and ductility in multimodal-structured Zr, Mater. Des. 34 (2012) 275–278.

[53] Y. Wang, M. Chen, F. Zhou, E. Ma, High tensile ductility in a nanostructured metal, Nature 419 (6910) (2002) 912–915.

[54] S. Nelson, L. Ladani, T. Topping, E. Lavernia, Fatigue and monotonic loading crack nucleation and propagation in bimodal grain size aluminum alloy, Acta Mater. 59 (9) (2011) 3550–3570.

[55] A. Magee, L. Ladani, T.D. Topping, E.J. Lavernia, Effects of tensile test parameters on the mechanical properties of a bimodal Al–Mg alloy, Acta Mater. 60 (16) (2012) 5838–5849.

[56] Y. Zhao, T. Topping, Y. Li, E.J. Lavernia, Strength and ductility of Bi-modal Cu, Adv. Eng. Mater. 13 (9) (2011) 865–871.

[57] D.K. Yang, P.D. Hodgson, C.E. Wen, Simultaneously enhanced strength and ductility of titanium via multimodal grain structure, Scr. Mater. 63 (9) (2010) 941–944.

[58] J.Y. Lee, J.H. Kim, S.I. Park, H.M. Lee, Phase equilibrium of the Ti–Cr–V ternary system in the non-burning β-Ti alloy region, J. Alloys. Compd. 291 (1) (1999) 229–238.
[59] H. Takahashi, S. Ohnuki, T. Takeyama, H. Kayano, The effect of irradiation and post-irradiation annealing on the yield stress and microstructure of vanadium-carbon alloys, J. Nucl. Mater. 96 (3) (1981) 233–242.
[60] Y. Zhao, P. Zheng, Y. Wei, H. Luo, W. Qian, G. Zhang, F. Li, M. Zhang, P. Zhang, Irradiation hardening and microstructure study of MAX-phase-dispersion-strengthened vanadium alloy under self-ion Irradiation. Metals, 2024.
[61] T. Sparks, D. Nguyen-Manh, P. Zheng, J.S. Wróbel, D. Sobieraj, M. Gorley, T. Connolley, C. Reinhard, Y. Wang, B. Cai, Mechanical characterisation of V-4Cr-4Ti alloy: tensile tests under high energy synchrotron diffraction, J. Nucl. Mater. 569 (2022) 153911.
[62] J.M. Cowley, X-ray measurement of order in single crystals of Cu3Au, J. Appl. Phys. 21 (1) (1950) 24–30.
[63] Y. Ishikawa, T. Yoshimura, Mechanically stimulated outgassing from stainless steel surface, J. Vac. Sci. Technol. A 9 (3) (1991) 2021–2024.
[64] P. Řepa, D. Orálek, Outgassing stimulated by deformation, Vacuum. 53 (1) (1999) 299–302.
[65] H.Y. Chang, R.K. Viswanadham, C.A. Wert, Age-hardening in the V-C and Nb-C systems, Metall. Trans. 5 (8) (1974) 1907–1917.
[66] D.R. Diercks, C.A. Wert, An electron microscopy study of carbide precipitation in vanadium, Metall. Trans. 3 (7) (1972) 1699–1708.
[67] Y.-Q. Chang, Q. Guo, J. Zhang, L. Chen, Y. Long, F.-R. Wan, Irradiation effects on nanocrystalline materials, Front. Mater. Sci. 7 (2) (2013) 143–155.
[68] O. El-Atwani, A. Alvarado, K. Unal, S. Fensin, J. Hinks, G. Greaves, J. Baldwin, S. Maloy, E. Martinez, Helium implantation damage resistance in nanocrystalline W-Ta-V-Cr high entropy alloys, Mater. Today Energy 19 (2021) 100599.
[69] Y. Zhang, R. Li, S. Diao, F. Wan, Q. Zhan, Plasticity improvement and radiation hardening reduction of Y doped V-4Cr-4Ti alloy, J. Nucl. Mater. 560 (2022) 153508.
[70] T. Miyazawa, T. Nagasaka, R. Kasada, Y. Hishinuma, T. Muroga, H. Watanabe, T. Yamamoto, S. Nogami, M. Hatakeyama, Evaluation of irradiation hardening of ion-irradiated V–4Cr–4Ti and V–4Cr–4Ti–0.15Y alloys by nanoindentation techniques, J. Nucl. Mater. 455 (1) (2014) 440–444.
[71] H. Luo, F. Luo, Y. Chen, J. Wang, Q. Liu, F. Li, Z. Xie, W. Lin, L. Guo, Effect of yttrium content on microstructure and irradiation behavior of V-4Cr-4Ti-xY alloys, J. Nucl. Mater. 559 (2022) 153480.
[72] K.-I. Fukumoto, Y. Kitamura, S. Miura, K. Fujita, R. Ishigami, T. Nagasaka, Irradiation hardening behavior of He-irradiated V–Cr–Ti alloys with low Ti addition, Quantum Beam Sci. (2021).
[73] K.-I. Fukumoto, Y. Zou, T. Nagasaka, R. Ishigami, Microstructural changes and irradiation hardening behavior of V-4Cr-4Ti alloys irradiated with He ions using flash-electropolishing, J. Nucl. Mater. 603 (2025) 155438.
[74] W.D. Nix, H. Gao, Indentation size effects in crystalline materials: a law for strain gradient plasticity, J. Mech. Phys. Solids. 46 (3) (1998) 411–425.
[75] W.C. Oliver, G.M. Pharr, An improved technique for determining hardness and elastic modulus using load and displacement sensing indentation experiments, J Mater Res. 7 (6) (1992) 1564–1583.